Insights into the interaction between defrosting seasonal ices and gully activity from CaSSIS and

K. Pasquon, S.J. Conway, M. Vincendon, M. Massé, J. Raack, A. Noblet, A. Grau Galofre, C. Morino, G. Munaretto, A. Lucchetti, et al.

Insights into the interaction between defrosting seasonal ices and gully activity from CaSSIS and HiRISE observations in Sisyphi Cavi, Mars

K. Pasquon[1], S. J. Conway[1*], M. Vincendon[2], M. Massé[1], J. Raack[3,4], A. Noblet[1], A. Grau Galofre[1], C. Morino[5], G. Munaretto[6], A. Lucchetti[6], M. Pajola[6], Stephen R. Lewis[7] and the CaSSIS team.

[1]Nantes Université, Université d'Angers, le Mans Université, CNRS UMR 6112 Laboratoire de Planétologie et Géosciences, France

[2]Institut d'Astrophysique Spatiale, CNRS, Université Paris-Saclay, France,

[3]Institut für Planetologie, Westfälische Wilhelms-Universität, Münster, Germany.

[4]Innomago GmbH, Ludgeristraße 110, 48143 Münster, Germany.

[5]Laboratoire EDYTEM, Université Savoie Mont Blanc, CNRS UMR 5204, Chambéry, France.

[6]INAF, Osservatorio Astronomico di Padova, Padova, Italy

[7]School of Physical Sciences, Open University, Milton Keynes, UK.

*corresponding author, susan.conway@univ-nantes.fr

Abstract

Martian gullies are surface features, typically composed of an alcove, a channel and a depositional apron. They have been extensively studied since their first observations in the 2000s and were initially attributed to the action of liquid water. Later studies highlighted that their activity is spatially and temporally correlated with the seasonal presence of surface CO_2 ice, suggesting a link between seasonal frost and gully activity. However, the exact mechanisms leading to gully formation are still under debate. Establishing whether or not gullies are formed by liquid water has important implications for Mars recent climate and habitability. Here, we study the evolution of seasonal frost and its connection to gully activity in Sisyphi Cavi, located in the southern circumpolar region (68°S - 74°S; 345°E - 5°E). The high latitude of this site allows for detailed temporal monitoring, owing to the high frequency imaging by spacecraft in polar orbits, largely unavailable for other martian gullies, hence this site has the potential to reveal new insights on gullies in general. In particular, we used repeat images from MRO HiRISE

(Mars Reconnaissance Orbiter, High Resolution Imaging Science Experiment) and TGO CaSSIS (Trace Gas Orbiter, Colour and Stereo Surface Imaging System). Our findings show that the general timing and characteristics of the defrosting patterns in Sisyphi Cavi follow seasonal patterns that are consistent from year to year. The timing of the start of defrosting and its temporal evolution are controlled by the overall orientation of the host hillslope, with equator-facing slopes defrosting before pole-facing ones and the steepest pole-facing slopes defrosting last. Gully alcoves defrost before channels and aprons located on the same hillslope independent of the orientation of the hillslope likely because the aprons have a lower thermal inertia than the alcoves that counteracts the orientation effect, which on pole-facing slopes would mean the alcoves should defrost last. We observe the presence of seasonal and ephemeral dark spots and flows which are interpreted to be a result of sediment deposition on top of the seasonal ice deposits, triggered by basal sublimation. Our observations suggest that the appearance of dark spots and dark flows can be spatially correlated with surface roughness, including presence of boulders, contrasts in material types, irregular lobes/levees and braiding caused by gully activity, and therefore could be used to help detect recently active gullies on Mars in areas with seasonal frost without the need of repeat imaging. Finally, we propose that presently observed gully activity in Sisyphi Cavi is driven by defrosted material flowing on to a frosted apron. We infer that the presence of a frosted apron could be common precursor for this type gully activity. We note that this activity only involves the mobilisation of loose materials and we have not observed any erosion of the wall rock present in Sisyphi Cavi.

1. Introduction

1.1. Gullies and seasonal frost

Martian gullies have been abundantly studied since they were first observed by Malin and Edgett (2000). Yet their formation mechanism is still under debate (e.g. Heldman and Mellon, 2004; Cedillo-Flores et al., 2011). Gullies are landforms typically composed of an alcove, a channel and a depositional apron, with a lengthscale of kilometres (Malin and Edgett, 2000; Harrison et al., 2015) and they are located on steep slopes spanning latitudes from 30° N/S to the polar caps (Conway et al., 2019a). They are generally present on crater walls and central peaks, fossae/valles walls or on sand dunes (Malin and Edgett, 2000; Dundas et al., 2012; 2015; 2019; Diniega et al., 2010; Hansen et al., 2011; Jouannic et al., 2012; Harrison

et al., 2015; Raack et al., 2015; Pasquon et al., 2019a), being particularly abundant in the southern hemisphere, where steep slopes are commonplace (e.g. Harrison et al., 2015). Gully morphologies are highly variable and include features which can have kilometre-wide alcoves and aprons as well as metres wide "linear" dune gullies (Dickson et al., 2007; 2012; Conway et al., 2011; Harrison et al., 2015; Pasquon et al., 2019a).

Many different hypotheses have been proposed for martian gully formation: liquid water from shallow groundwater aquifers (Malin and Edgett, 2000; Mellon and Phillips, 2001; Heldmann and Mellon, 2004; Heldmann et al., 2005; Malin et al., 2006), deep groundwater sources (Gaidos, 2001; Hartmann, 2001), melting of shallow ground ice (in the form of pore ice or excess ice; Costard et al., 2002; Reiss and Jaumann, 2003; Mangold et al., 2003, 2010; Miyamoto et al., 2004; Balme et al., 2006; Reiss et al., 2010; Conway et al., 2011a; Jouannic et al., 2012, 2015; Conway and Balme, 2016), snow/icemelt (Lee et al., 2001; Christensen, 2003; Dickson et al., 2007; Védie et al., 2008; Hauber et al., 2011; Williams et al., 2009; Khuller & Christensen, 2021), or dry mass wasting (Treiman, 2003; Shinbrot et al., 2004), brines (Knauth and Burt, 2002; Ojha et al., 2015; Massé et al., 2016), frosted granular flow (CO_2, H_2O) (Hugenholtz, 2008), CO_2-supported debris flows (Hoffman, 2002; Ishii and Sasaki, 2004; Di Achille et al., 2008; Diniega et al., 2010; Cedillo-Flores et al., 2011; Dundas et al., 2012; 2015; 2019; Pilorget and Forget, 2016), and release of liquid CO_2 (Musselwhite et al., 2001). For a full review see Conway et al. (2019b).

Some gullies are active today, including at times of the year when the martian surface is at its coldest and CO_2 ice is condensed on the surface, suggesting that they are triggered by seasonal processes related to ice (e.g., Dundas et al., 2010; Diniega et al., 2013; Raack et al., 2015; Pasquon et al., 2019b). Such seasonal processes are generally attributed to CO_2 sublimation driven by solar radiation (e.g., Kieffer, 2000; 2007; Kieffer et al., 2006; Hansen et al., 2011). The seasonal CO_2 and water ices start to accumulate on the surface during autumn and sublimate away the following spring. During winter, these deposits: i) cover all surfaces above ~ 60° latitude, ii) are discontinuous from 40° to 60° of latitude (Schorghofer and Edgett, 2006; Vincendon et al., 2010; Diniega et al., 2013), and iii) are limited to pole-facing slopes nearer the equator (Lange et al. 2022; Dundas et al., 2015, 2019, Vincendon et al., 2010; Khuller, et al., 2021; Piqueux et al., 2016). Ice deposits can be up to meters thick near the poles (Smith

et al., 2001), to sub-centimetre in thickness at lower latitudes (Vincendon, 2015). Most ice deposits are composed of CO_2 (~centimetres) (Diniega et al., 2013; Dundas et al., 2015), whereas H_2O is a minor component (~micrometres) (Kereszturi et al., 2009; Gardin et al., 2010; Vincendon et al., 2010a; 2010b). To simplify terminology, in this paper we use the term "frost" to describe the seasonal ice deposits of Mars.

1.2. Sisyphi Cavi and gully activity

Sisyphi Cavi is a site with an anomalously high concentration of gullies for its latitude (Harrison et al. 2015) located in the southern circumpolar area (68°S - 74°S; 345°E - 5°E). This is likely caused by a higher frequency of steep slopes than typical of this latitude (Conway et al. 2019a), due to the occurrence of numerous steep-sided, flat-floored depressions, generally several hundred kilometres across and more than 1 km deep (Tanaka and Scott, 1987). Conway et al. (2019a) defined steep as being >20° at the ~1.5 km length scale allowed by the Mars Orbiter Laser Altimeter gridded data. Raack et al. (2020) showed the slope at length scales of 100 m exceeds 30° at the top of the hillslopes in Sisyphi Cavi and that the steepest portion of the hillslope was consistently located at the top. Hence, throughout this paper we make the assumption that the steepest part of the hillslope is located in the upper part. The formation of these depressions, which are incised into Amazonian surfaces (Tanaka and Scott, 1987), is not completely understood (e.g., Raack et al., 2020). Gullies are present over large continuous swathes of the walls of these depressions (Raack et al., 2020).

Previous work by Raack et al. (2015, 2020) considered the timing of gully activity in Sisyphi Cavi. They found that sediments were transported down the gully and deposited over the apron in 35 gullies (out of a total of 19,827 gullies). None of these observation revealed erosion of the wall rock present in Sisyphi Cavi by these flows. Using spectral observations and numerical modelling, Raack et al. (2015) showed that the surface ice deposit during the period of gully activity consists of a translucent slab of CO_2 ice with minor amounts of H_2O ice. Gully activity occurs at the end of the spring, during the final stages of defrosting when some surfaces are already fully ice-free. They suggested that activity is driven by dry flows mobilised over a sublimating CO_2 ice slab, similar to the mechanism proposed by Cedillo-Flores et al. (2011). Raack et al. (2020) refined this model, suggesting an accumulation of

material within gully channels via small dry flows on top of the ice. When a critical mass sediment is reached on top of the slab ice, the sediment flows down the still frosted gully on top of the sublimating ice or as a mixture of dry material and sublimating ice as a flow. This accumulation phase means more sediment would be mobilised, explaining the observable thickness of the flow deposits.

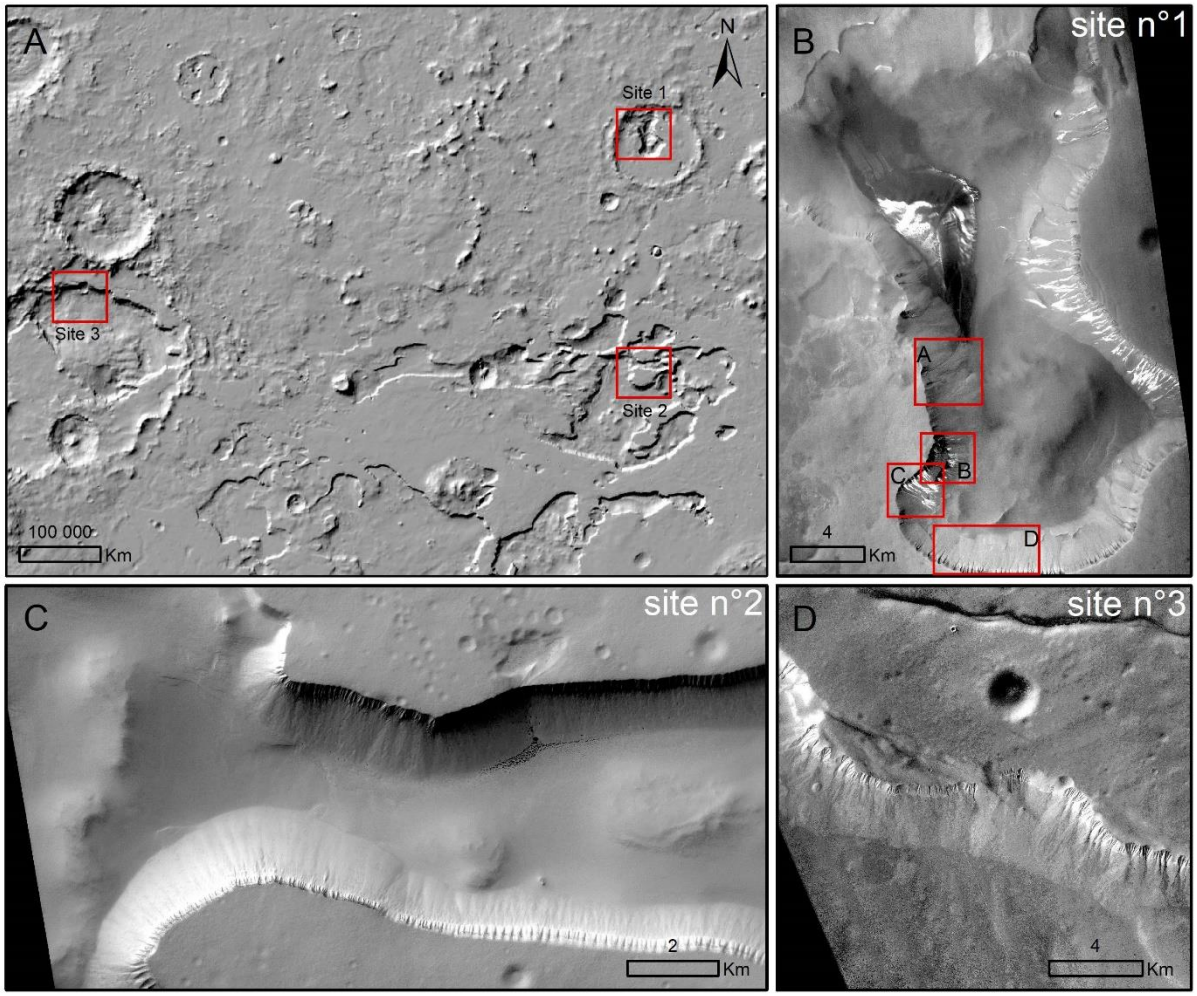

Fig. 1: Map of Sisyphi Cavi on Mars: A) overview images of the 3 sites studied in this paper (Mars Orbiter Laser Altimeter, hillshaded relief map), B) Site n° 1, where red boxes delimit the subsites A-D: 68.5°S; 1.3°E (ConteXT camera – CTX - image: B08_012741_1115_XN_68S358W), C) Site n°2: 70.9°S, 1.2°E (CTX image: B05_011673_1092_XN_70S358W); D) Site n°3: 69.4°S; 347°E (CTX image: D04_028618_1103_XN_69S013W). CTX Credit NASA/JPL/MSSS.

1.3. Dark spots and dark flows

Ephemeral dark spots were reported for the first time by Malin (1998). These are low albedo spots (generally circular) that can measure up to several metres in diameter (Kereszturi et al., 2009, 2010) and are linked to seasonal CO_2 ice deposits (Gardin et al., 2010; Kereszturi et al., 2009, 2010; Möhlmann and Kereszturi, 2010; Diniega et al., 2021). Dark spots usually appear between the middle of the winter and early spring and disappear each year in late winter/early summer (Kereszturi et al., 2009). The prevailing hypothesis for dark spot formation is the accumulation of material following the ejection of dust and sand from a CO_2 gas jet (Kieffer et al., 2006; Kieffer, 2000, 2007; Piqueux and Christensen, 2008). These gas jets are thought to form as follows: In winter CO_2 frost is deposited on the surface, quickly sintering and producing an impermeable slab that becomes translucent to visible radiation. After mid-winter the sun's rays penetrate the translucent ice and heat the underlying substrate, causing the CO_2 ice to sublimate at its base. An over-pressure, due to the CO_2 gas that accumulates, occurs under the ice layer and cracks the ice (Piqueux et al. 2003; Kieffer et al. 2006; Piqueux and Christensen 2008; Portyankina et al., 2011). Degassing occurs through these cracks and particles are entrained by the gas and redeposited on the surface of the ice (e.g. Piqueux et al., 2003; Kieffer et al., 2006; Portyankina et al., 2011). When dark spots appear on a sloping surface, they can evolve into "dark flows" which are dark features that can incrementally elongate downslope (Kereszturi et al., 2009; 2010; Gardin et al., 2010; Jouannic et al., 2019). Dark spots and flows are not associated with measurable material transport, so it is inferred that only dust or very minor amounts of sand are mobilised. Dark flows have been also interpreted to result from flowing brines (Möhlmann and Kereszturi, 2010; Kereszturi et al., 2011). However, their consistent association with CO_2 spectral signatures (Pommerol et al., 2013) in a wide range of environments and observations of fast flow speeds inconsistent with viscous brine (Gardin et al., 2010) suggest they may simply be another type of gas supported flow.

Dark spots and dark flows are visible each spring on the slopes, gullies and dunes of Sisyphi Cavi. They preferentially occur on dunes and inside gully channels and aprons (Raack et al., 2015; 2020). No perennial morphological changes have been associated with the activity of dark spots and dark flows in Sisyphi Cavi (Raack et al., 2015; 2020). Here, we also document their occurrence because their link with active gullies is ambiguous.

1.4. Objectives of this study

Previous studies (Raack et al., 2015; 2020) showed that the activity of gullies in Sisyphi Cavi occurs before the seasonal frost disappears from the surface, and thus suggest that a relationship likely exists between gully activity and springtime defrosting. Here we perform a detailed study of seasonal frost evolution on the slopes of Sisyphi Cavi (68-74°S; 345°-5°E) (Fig. 1A), exploring the relationship between gully activity and frost occurrence. We focus on two main points: 1) Investigating the changing appearance of the seasonal frost through the winter and spring before gully activity occurs, to build intuition on the environmental factors leading to gully activity; and 2) the sequence of events and their timing during defrosting, to better understand the potential triggers and conditioning factors for activity.

2. Methods

We based our study on the analysis of HiRISE (High Resolution Imaging Science Experiment; McEwen et al., 2007) and CaSSIS (Colour and Stereo Surface Imaging System; Thomas et al., 2017) image data. The HiRISE camera is aboard NASA's MRO (Mars Reconnaissance Orbiter) spacecraft, and acquires images with a spatial resolution of 0.25-1 m/pixel and three filters (RED, BLU and NIR centred on 694, 536 and 874 nm respectively) (McEwen et al., 2007). The CaSSIS camera is on board ESA's TGO (Trace Gas Orbiter) spacecraft. CaSSIS acquires images with a resolution of ~4.6 m/pixel and four possible colour filters (BLU, PAN, RED and NIR centred on 497.5, 677.4, 835.4 and 940.2 nm respectively) (Thomas et al. 2017).

Given the large dimensions of our study area (68°-74°S; 345°-5°E) we divide the region into "sites", with smaller "areas" defined within each site (Fig. 1). Image data available for Sisyphi Cavi have a spatially discontinuous time coverage with some sites having only one or two images. We divide the region in 3 sites, each containing between 4 and 20 gullies, located at: 1) 68.5°S and 1.3°E (Fig. 1B), 2) 70.92°S and 1.2°E (Fig. 1C) and 3) 69.4°S and 347°E (Fig. 1D). Although these sites form the majority of our data analysis, we also use images located elsewhere in Sisyphi Cavi as illustrative examples. A summary of the images used is provided in Supplementary Table S1.

To describe the timing of events in this paper, we use the solar longitude (Ls) of the first image where we observe the feature/ activity appear and the Ls when we observe it for the last time. So, the

disappearance of the feature occurs after the last Ls provided, but before the Ls of the next image in the sequence (all sequences are visible in the Supplementary Table S1) for the same Mars Year. As interannual variability in the timing of defrosting (Piqueux, et al., 2015) is less than the typical time gap between images, we sometimes group data from different Mars years to form more complete datasets. The events documented in this paper include: appearance of dark spots, appearance of dark flows, and the assessment of the continuity of frost cover.

Assessing frost/ice cover from optical images is challenging because of the transparency of slab CO_2 ice in visible wavelengths and up to 25 cm of CO_2 ice can accumulate before the surface is masked in the visible wavelengths (Singh and Flanner, 2016). We address this by using features/patterns in optical data observed by other researchers, where these researchers used spectral datasets to confirm the presence of frost. We infer the presence of transparent ice, by the fact that surface features such as ripples and boulders can be weakly observed on the surface, and the surface shows dark spots and flows indicative of the presence of slab ice (Andrieu et al. 2018; Kieffer et al., 2006; Kieffer, 2000, 2007; Piqueux and Christensen, 2008). Brightening of the seasonal ice cover at a given location just prior to its retreat has been noted in previous publications (e.g. Langevin et al. 2007; Calvin et al. 2017) and is thought to represent break-up of the CO_2 to smaller grainsizes or deposition of water ice frost cold trapped by the CO_2. We infer that on partially defrosted surfaces, the remaining CO_2 ice acts as a cold trap for water vapour which in turn presents a highly visible, bright surface frost, which contrasts with the lower albedo of the defrosted surfaces. We classify images as completely defrosted when no remaining bright patches can be observed on any surface. We are reasonably confident with this interpretation as these images are always towards the end of spring in our time series and these images which occur later than the time of retreat of the seasonal cap at this latitude as detected by other researchers using thermal and/or spectral data (Brown et al., 2010; Piqueux, et al., 2015).

We highlight that site n°1 has the best coverage, with 59 HiRISE and 11 CaSSIS images available, so we focus most of our analysis on this site. As Supplementary Table S1 shows, there is good temporal sampling of this region spanning from mid-winter to summer (from Ls 158.4° to Ls 349.5°). However, the lack of images from the middle of summer to the start of winter (from Ls 349.5° to 158.4°) prevented

us from studying the emplacement of the seasonal frost. We further divide the site n°1 into several areas, (A to D, Fig. 1B) to distinguish different parts with different hillslope orientations.

3. Results and interpretations

3.1. Patterns in seasonal defrosting

In this section, we only report results from site n°1 (68.5°S and 1.3°E, Fig. 1B) due to the better multi-temporal image coverage (Supplementary Table S1), unless otherwise indicated.

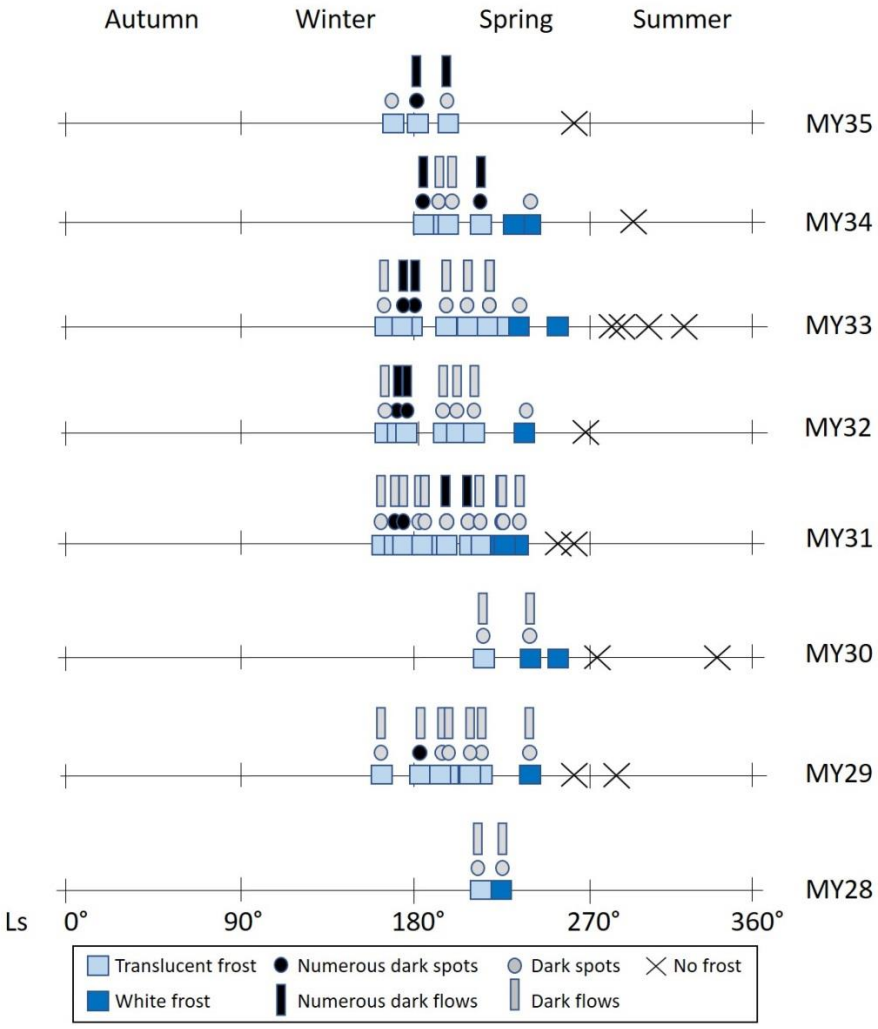

Fig. 2: Defrosting timing at site n°1, area C (68.5°S and 1.25°E see Fig. 1AB) for martian years 28 to 35. Each symbol represents the timing of the image given in Supplementary Table S1.

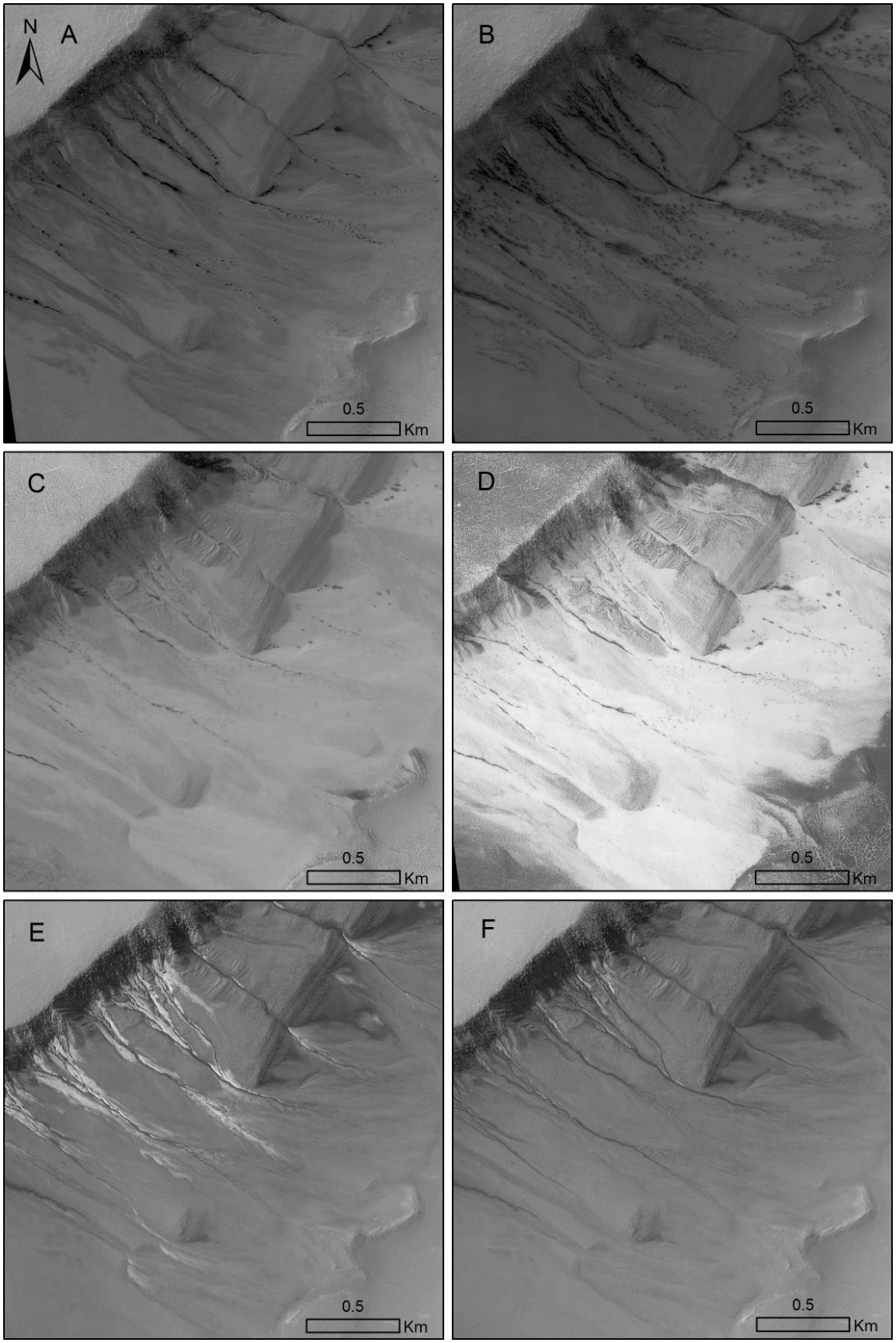

Fig. 3: Typical seasonal frost evolution in Sisyphi Cavi for site n°1, area C (68.5°S; 1.3°E)A) Dark spots and flows visible mainly in the gully channels and on the aprons, ESP_028446_1115, Ls 158.4°. B)

Dark spots and flows are more numerous than in panel A, being relatively dense in the gully channels and more prevalent on the aprons, ESP_028802_1115, Ls 173.3°. C) Faded dark spots and fans still visible and portions of equator-facing slopes in the alcoves are starting to defrost, ESP_029936_1115, Ls 225.6°, D) Frosted surfaces on this image appear bright, with defrosted surfaces appearing dark. Dark spots and flows are visble on the gully channels and aprons, ESP_030147_1115, Ls 235.9°, E) Most of the terrain in the image is defrosted with bright frost remaining only around the channels and some parts of the apron, ESP_021589_1115, Ls 248.7°, F) Only small patches of bright frost remaining in parts of the gully channel near the alcoves, ESP_021668_1115, Ls 252.6°. Image credit: HiRISE NASA/JPL/UofA. Note that each image was individually contrast-stretched.

3.1.1. General patterns in seasonal defrosting

We first focus our analysis on areas C and D within region 1, which have the highest temporal and spatial availability of image data. Regions C and D (Fig. 1B) contain 59 and 57 HiRISE images respectively, spanning Martian Years (MY) 28 to 35, with 7-13 images available for each year.

In each martian year, we consistently observe the following sequence of events leading to defrosting, with area C lagging tens of Ls behind area D (Supplementary Table S2):

- We observe numerous dark spots and dark flows on top of the translucent frost, around Ls 160-230° (Figs. 2, 3AB; Supplementary Table S2). The frost is considered as translucent, because underlying features (e.g., boulders, alcoves, or channels) can still be seen.
- After this, the frost becomes "brighter" with fewer or absent dark spot(s) and dark flow(s) (Figs. 2; 3CDEF; Supplementary Table S2). This brightening has been noted in previous publications (e.g. Langevin et al. 2007), but could be attributed to changes in overall image contrast. In either case it indicates the break-up of the translucent frost (Fig. 3C-F).
- From Ls 170° to 225°, the frost becomes visually patchy and discontinuous and only some small patches are visible by Ls 225° (Figs. 2, 3 DEF; Supplementary Table S2).
- Defrosting is complete at around Ls 250-300° (Fig. 2; Supplementary Table S2).

Dark spots and dark flows never appear when frost becomes patchy. They are first visible only when frost seems to be continuous.

248

249

3.1.2. Defrosting patterns of gullies

Here, we report on the frost occurrence and distribution within gullies, including the alcoves, channels, and aprons, during winter and spring in areas C and D (region 1). We observe a consistent sequence of events across martian years, as shown in Supplementary Table S3:

- All surfaces are frosted until Ls ~220° (Figs. 2; 3AB; Supplementary Table S3),
- Then, alcoves begin to defrost, while areas surrounding the gullies begin to defrost starting at ~Ls 230° (Supplementary Table S3). At the same time or just afterwards the channels and aprons begin to defrost.
- The areas around gullies become completely defrosted as early as Ls 210° and as late as Ls 247° (Supplementary Table S3),
- The alcoves are completely defrosted. Then the channel and aprons are the last to defrost at ~Ls 250° (Supplementary Table S3), where some patches of late persistent frost remain visible at the bottom of alcoves and inside the channels (Fig. 3F),
- All surfaces are defrosted around Ls 240-300° i.e., between the middle of spring to the beginning of summer (Fig. 2; Supplementary Table S3).

Within this sequence, gully alcoves defrost before channels and aprons on areas C and D (Fig. 3DE; Supplementary Table S3). Yet some patches of frost persist inside the channel and at the bottom of the alcove (Fig. 3F). In general, gullies defrost later than their surrounding terrain (Fig. 3DE; Supplementary Table S3), with the notable exception of sandy areas, such as dunes.

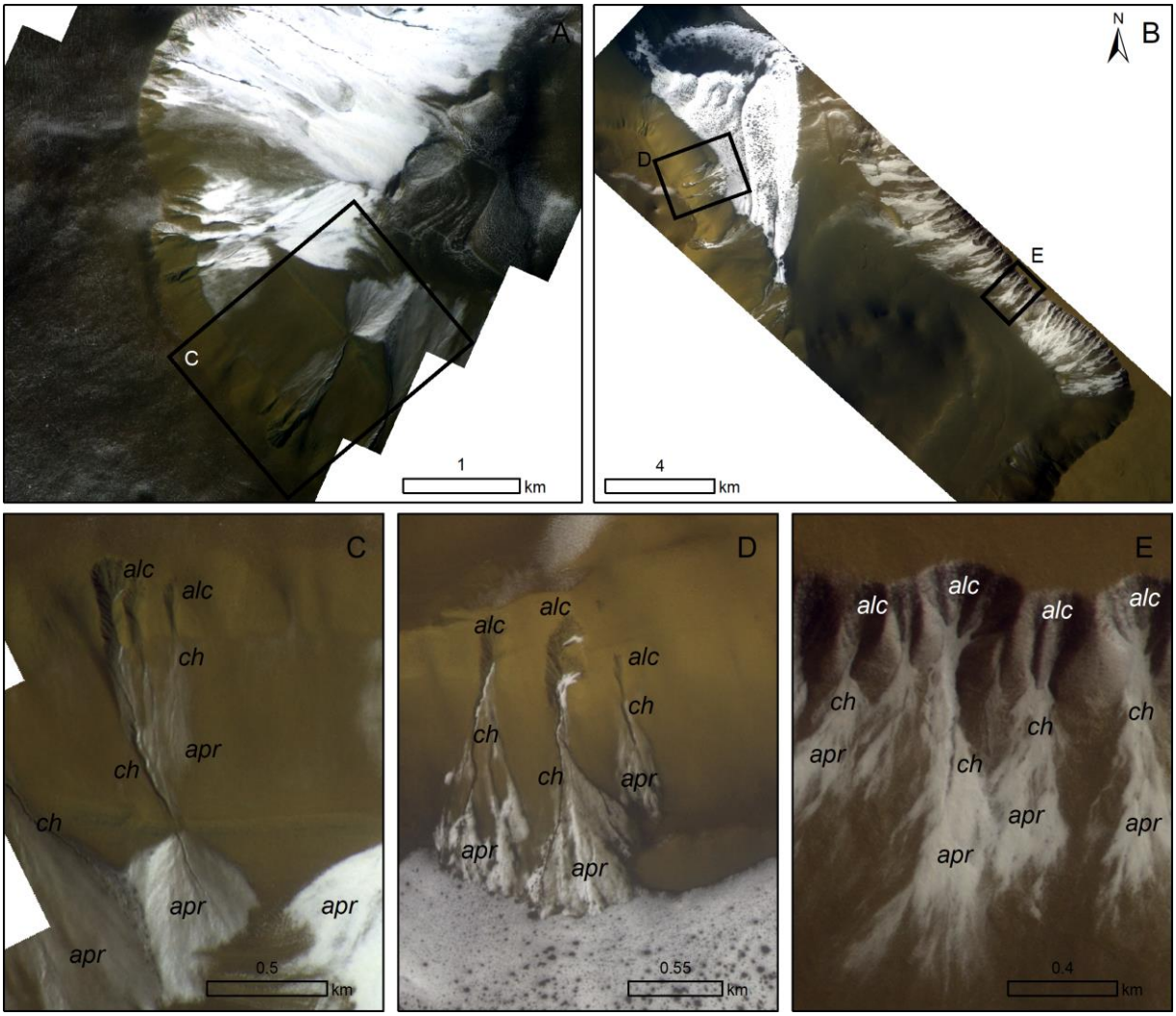

Fig. 4: Influence of gully orientation on seasonal frost deposits in Sisyphi Cavi (site n°1: 68.5°S; 1.3°E). Synthetic RGB CaSSIS images using the PAN and BLU channels, where defrosted surfaces appear red and frosted surfaces white: A and C) MY35_011760_288, Ls 332°, B, D and E) MY34_003464_256_1, Ls 342°. Panels A and B are context views for close-ups on individual gullies in C-E, where alc = alcove, ch = channel and apr = apron. CaSSIS credit: ESA/Roscosmos/Unibe. Note that each image was individually contrast-stretched.

3.2. Effects of slope orientation on defrosting

We now report the results of studying the timing of defrosting for gullied slopes with differing orientations and different orientations of slope facets within their alcove and channels. We include observations from MY31 for site n°1 (68.5°S, 1.3°E; Figs. 4, 5 and 6), and site n°2 (69.5°S, 347°E; Fig.

7). For site n°1, area A has a slope orientation of 80°-85°N, area B: 95°-105°N, area C: 130°-140°N, and area D: 0° - 10°N (Fig. 1B). For site n°2 (Fig. 7), we divide the gullies observed into two groups according to their slope orientation. Slopes in gully group 2A are oriented 225° with respect to north, on average, whereas group 2B has an orientation of 200°.

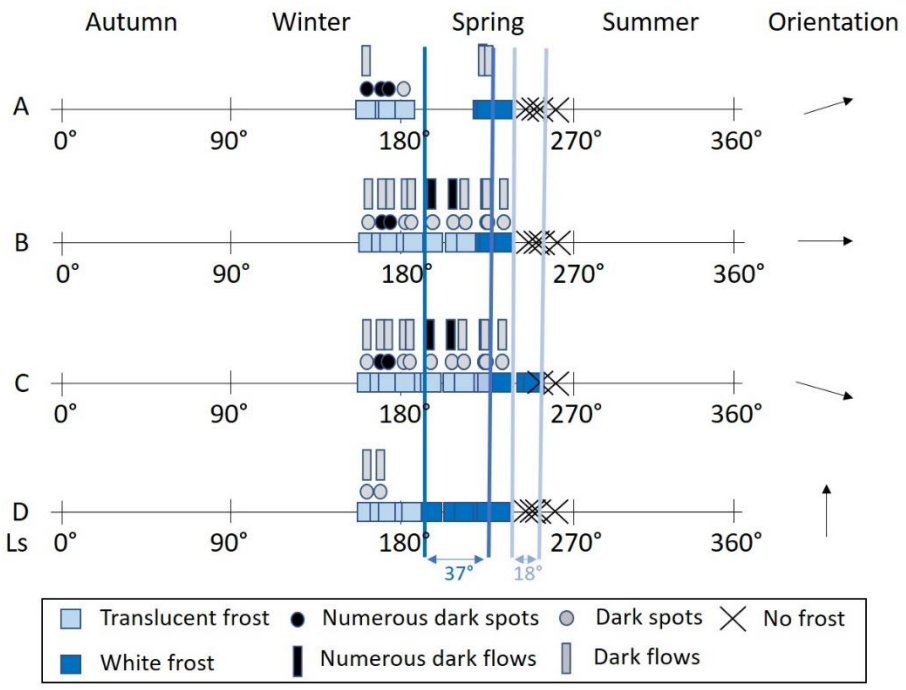

Fig. 5: Defrosting sequence for areas A, B, C and D which have different orientations - site n°1 (68.5°S; 1.3°E, MY31). Blue lines highlight the inter-site variability of the timing of the end of translucent frost (dark blue lines) and of the end of defrosting (light blue lines), which is most extreme between equator-facing area D and slightly pole-facing area C. Each symbol represents the timing of the image given in Supplementary Table S1.

For each slope orientation, we observe the same sequence of seasonal defrosting and associated features for each of the areas A, B, C and D, as already described in section 3.1.1, with the detailed time intervals reported in Supplementary Table S4 and on Fig. 5. However, the onset of events in each area is offset in time. For example, there is a lag of 37° solar longitude between the appearance of "bright" frost in area C compared to area D (Fig. 5; Supplementary Table S4), and we observe a lag of 18° solar longitude in the complete defrosting of area C compared to area D (Fig. 5; Supplementary Table S4).

We also observe differences in seasonal frost patterns within gullies (e.g., on the channel flanks) that are related to the orientation of these slope facets, as shown in Fig.6 and Supplementary Table S3 for areas A, B, and C in MY31 and in Figure 7 for site n°2. In summary, equator-facing alcove facets start to defrost first, followed by equator-facing channel facets and parts of the surrounding terrain. Equator-facing alcove facets can be completely defrosted while pole-facing ones are only starting to defrost. On the contrary, pole-facing alcove and channel facets are the last to defrost. Slight east (or west) deviations on an equator-facing slope facet delay initial and complete defrosting, and conversely advance pole-facing slope facet defrosting.

In general, the timing of defrosting depends on slope orientation (Supplementary Table S4), and the sequence of events and the distribution of remaining frost remains consistent across regions. (Figs. 4, 7; Supplementary Table S4). An equator-facing slope always defrosts before a pole-facing slope for the same material type and slope angle (Figs. 6, 8; Supplementary Table S5). Yet, the orientation of slope facets inside an alcove or a channel causes differences in the relative timing of defrosting (Figs. 6, 8; Supplementary Table S5). Finally, gully-alcoves always defrost before channels and aprons regardless of gully orientation (Supplementary Tables 3, 4 and 5).

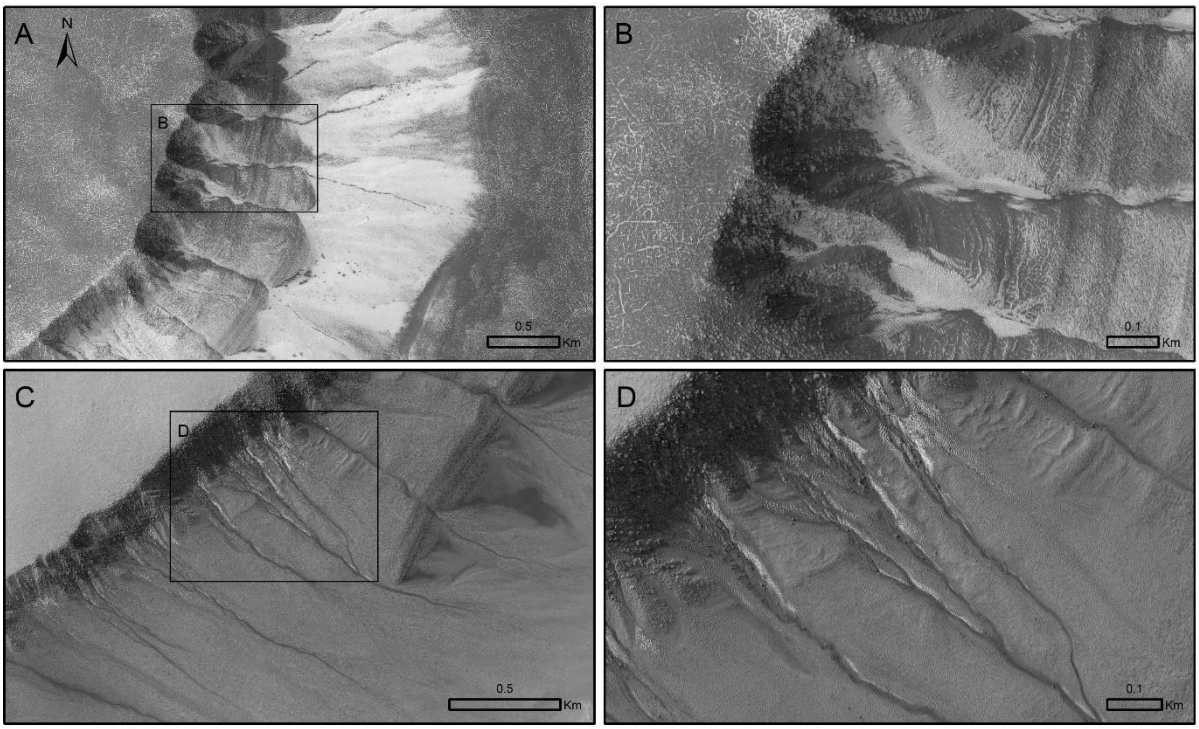

Fig. 6: Seasonal frost distribution inside gullies for site n°1 (68.5°S, 1.3°E), areas B and C: A) only equator-facing slope facets within the alcoves are defrosted. Area B, HiRISE image ESP_030147_1115, Ls 235.9°, MY31; B) Zoom in on part of the HiRISE image in panel A; C) The end of the seasonal defrosting, frost is still present on slope facets that are oriented towards the pole. Area C, HiRISE image: ESP_021668_1115, Ls 252.6°, MY30; D) Zoom in on part of the HiRISE image in panel C. Image credit NASA/JPL/UofA. Note that each image was individually contrast-stretched.

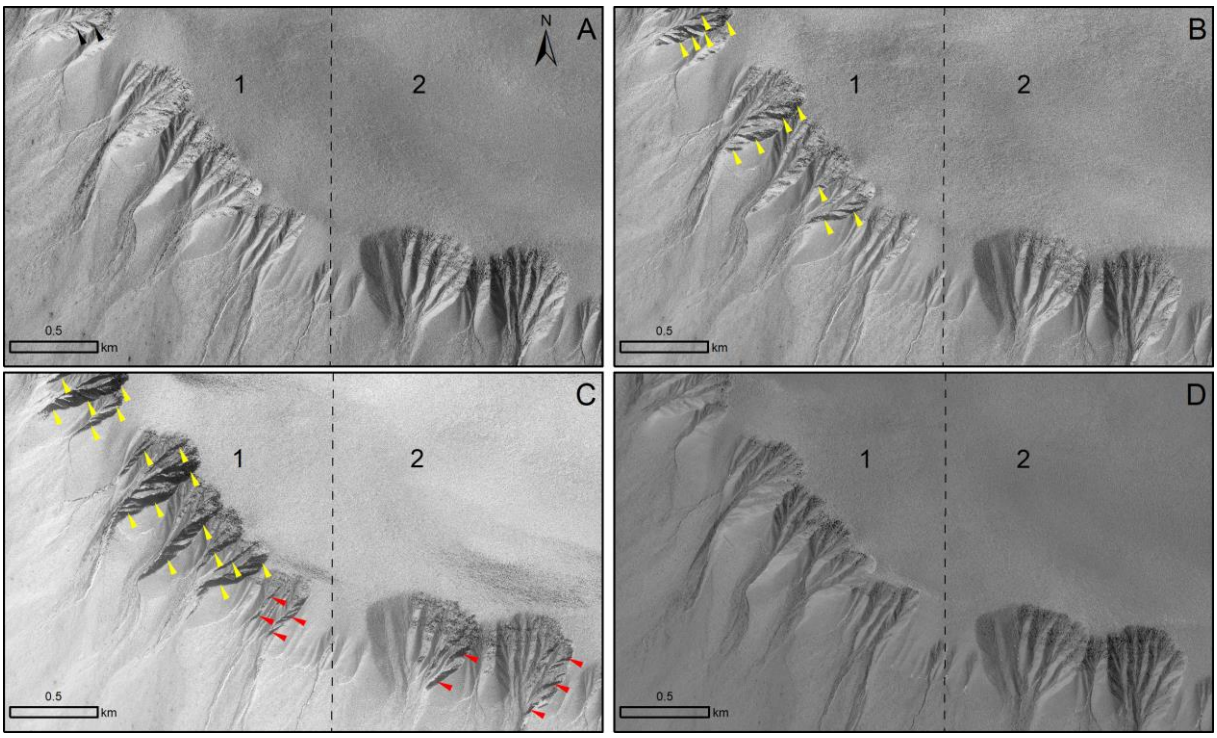

Fig. 7: Influence of slope orientation on the seasonal frost distribution at site n°3 (69.4°S, 347°E). The images are split into two parts by a dashed line in order to highlight the differences between gullies with different overall orientations: A) All surfaces are frost covered (parts 1 and part 2) except a couple of directly north facing facets highlighted by black arrows, HiRISE image ESP_029686_1105, Ls 213.6°; B) In part 1 defrosting is only visible on slope facets in the gully alcoves facing north-east (yellow arrows), and all of part 2 remains frosted. HiRISE image ESP_029897_1105, Ls 223.7 °; C) In part 1 defrosting is advanced within alcove facets facing north-east (yellow arrows)and is starting on facets facing east-north-east (ENE, red arrows) and in part 2 alcove facets facing east-north-east (red arrows) begin to defrost. HiRISE image ESP_030108_1105, Ls 234 °; D) All surfaces are defrosted. HiRISE

image ESP_030609_1105, Ls 258.8°. Image credit: NASA/JPL/UofA. Note that each image was individually contrast-stretched.

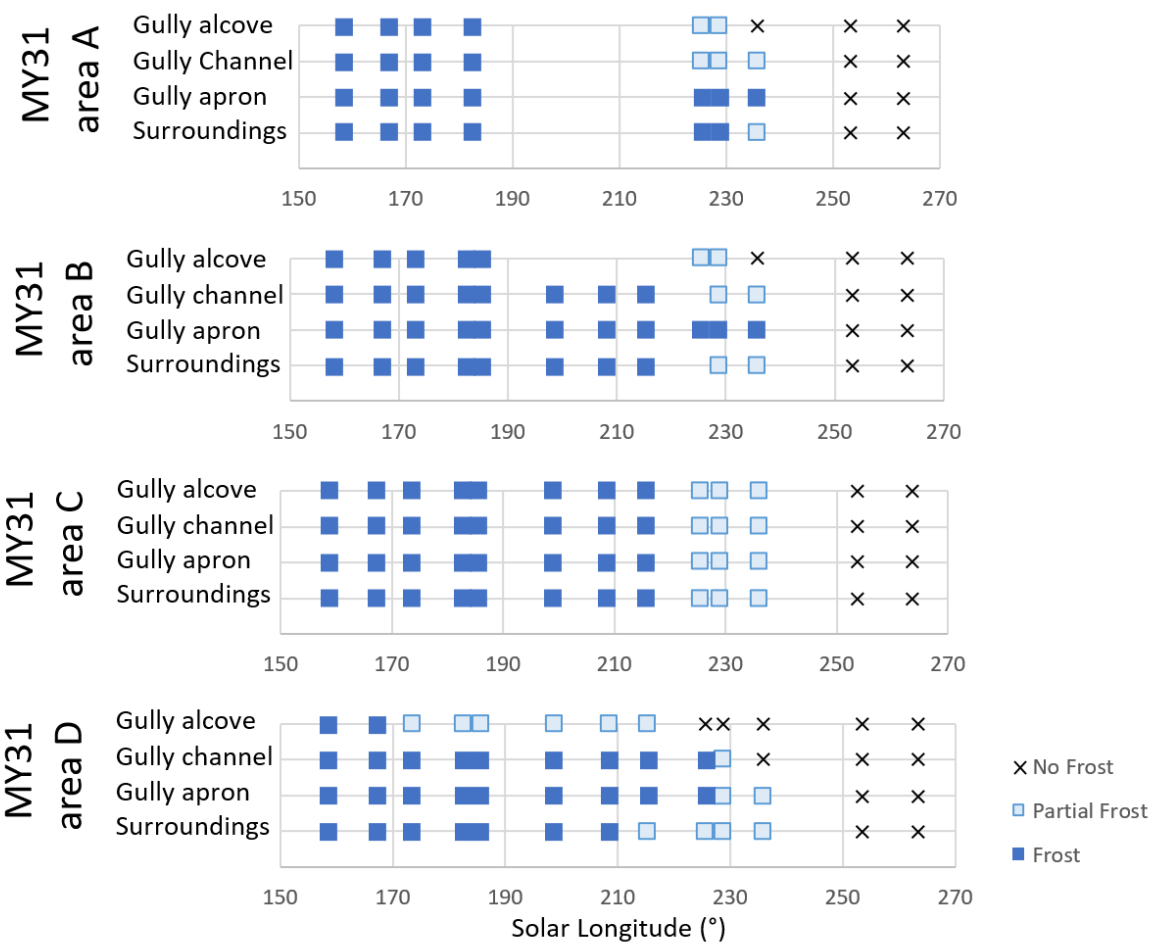

Fig. 8: presence of frost on different parts of the gully systems and terrain immediately surrounding the gullies for Site n°1 areas A-D.

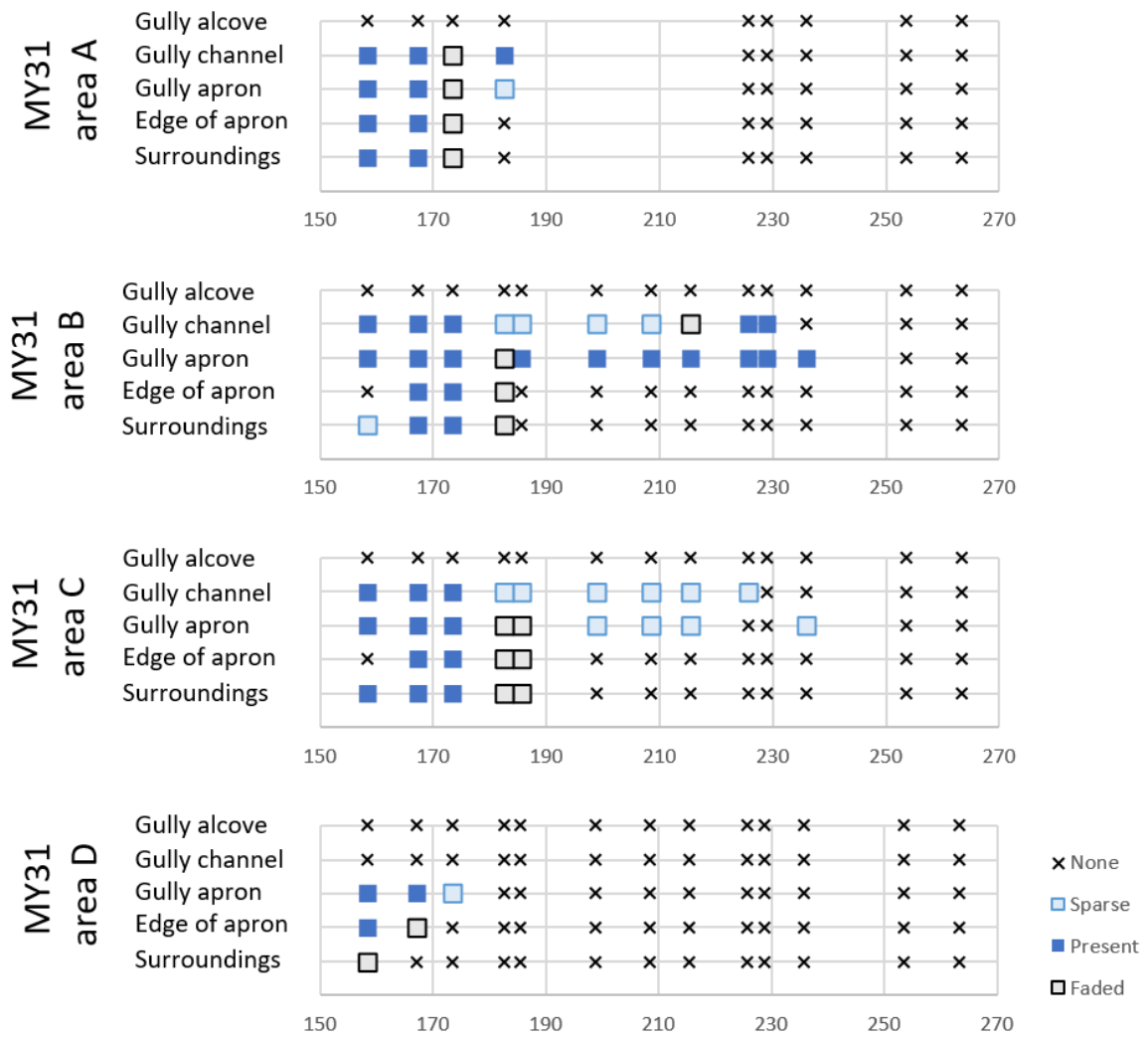

Fig. 9: Presence of dark spots and flows on different parts of the gully systems and terrain immediately surrounding the gullies for Site n°1 areas A-D.

3.3. Effect of surface type on defrosting

We next interrogate the relationship of dark spots and dark flows with surface roughness and gully activity using HiRISE and CaSSIS data. We find that surface roughness at the meter scale may influence the number of dark spots, and possibly dark flows present on the surface. We find that surface roughness is present in the form of boulders, depositional and erosional elements including braiding; levees, lobes. For this analysis we focus on the 3 sites shown in Fig. 1, located at: 1) 68.5°S and 1.3°E, 2) 70.92°S and

1.2°E and 3) 69.4°S and 347°E. Before considering the effect of surface roughness, we describe our general observations of dark spots and dark flows in Sisyphi Cavi.

3.3.1.Evolution of dark spots and dark flows in Sisyphi Cavi

We studied the presence and distribution of dark spots and dark flows in MY31 for areas A, B, C and D in site n°1. Dark spots and dark flows do not appear in gully alcoves in areas A, B or C, whereas both features are present in the channels from Ls 158.4° to Ls 228.8°, on the gully-apron from 158.4° to 235.9°, on the gully apron terminations from 167.2° to 185.5° and on the terrain around gullies from Ls 158.4° to 185.5° (Fig. 9; Supplementary Table S6). In contrast, dark spots appear on the terrain surrounding gullies and on gully aprons in area D at Ls 158.4° (Fig. 9; Supplementary Table S6). At Ls 167.2°, dark spots that were clearly visible in the previous image appear faded, whereas new dark spots appear on the smooth apron surfaces (Fig. 9; Supplementary Table S6). At Ls 173.3° nearly all dark spots appear faded, and at Ls 182.6° all dark spots have disappeared (Fig. 9; Supplementary Table S6).

Dark spots and dark flows are visible between the middle/end of winter to the middle/end of spring in Sisyphi Cavi (Figs. 2, 3ABCD, 9; Supplementary Tables 2 and 6). They are distributed non-homogeneously on all surfaces, with a spatial distribution that appears roughly similar from one martian year to the next, hinting at their preferential emplacement in given locations. Timing-wise, the appearance of dark spots and dark flows does not follow a reproducible pattern from year to year, and they do not have the same morphology, size, or lifetime (Fig. 3ABC, 9; Supplementary Tables 2 and 6). For a given slope with gullies sharing all the same overall orientation, several generations of dark spots may appear throughout the same martian year (Fig. 3ABC, 9; Supplementary Tables 2 and 6).

3.3.2. The role of surface roughness and substrate on the onset of dark spots and flows

Boulders are common on slopes in the Sisyphi Cavi region (Fig. 10), sourced from a layer that appears at the same elevation as gully alcoves. These boulders measure from 1 m^2 (the limit of HiRISE resolution) to nearly 30 m^2. These decametre-scale boulders are preferential locations for dark spot

formation (Fig. 10), and their occasional evolution into dark flows (Figs. 10CD). In our study region, the majority of visible boulders are associated with dark spots.

Dark spots (and sometimes dark flows) cluster on the floor of alcoves, in the channel, and/or on the apron as shown in Fig. 11. These surfaces are rougher than the surrounding terrain, having more boulders, but also having braided sections with metre-scale scarps and irregularities where aeolian smoothing seems to be less prevalent and we interpret this as being representative or more recently active areas (following Dundas et al. 2019).

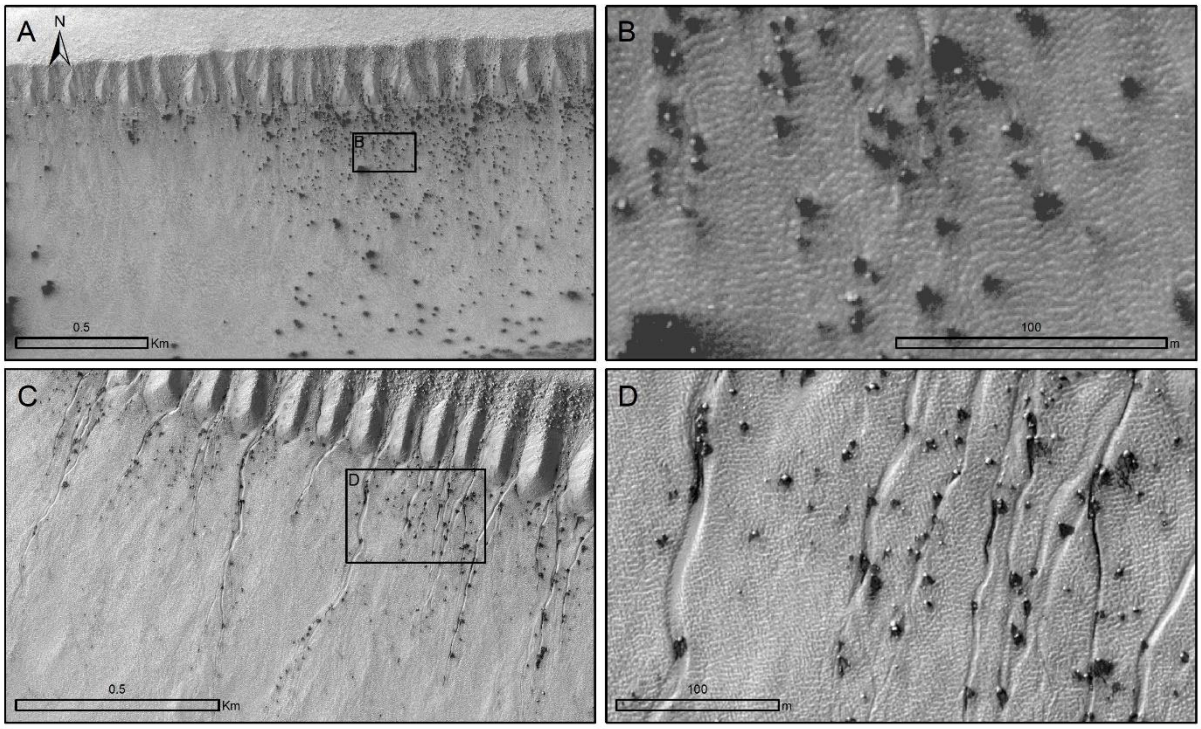

Fig. 10: Relation between boulders and dark spots/dark flows for site n°2 (70.7°S, 1.5°E). A) The west part of the image has few boulders, and correspondingly few dark spots, on the east part of the image there are more boulders and more dark spots. HiRISE image: ESP_028868_1090, Ls 176.2°, B) Zoom in on panel A which shows that each boulder correspond (on average) to a dark spot, C) Boulders and associated dark spots/dark flows concentrated along gullies are visible, HiRISE image: PSP_003353_1090, Ls 249.1°, D) Zoom in on part of panel C which shows the relation between the position of boulders and the presence of dark spot/dark flows. Image credit: NASA/JPL/UofA. Note that each image was individually contrast-stretched.

Contrasts in surface roughness as well as substrate composition and physical properties seem to facilitate the onset of dark spots. For example, the transition between apron and hillslopes host numerous dark spots (Fig. 12CD), which aids in the identification of this transition without having to zoom-in. Another example where dark spots concentrate is at the boundary between a sandy surface and the surrounding terrain, where they also sometimes evolve into dark flows if the terrain is sloping (Fig. 12AB).

In summary, we observe that the presence of metre-scale surface roughness produces a higher number of dark spots and dark flows in winter and spring (Figs. 10, 11 12). In Sisyphi Cavi, this roughness takes the form of: 1) boulders (Fig. 10), 2) braided gully surfaces (Fig. 11) and 3) contrasts in substrate properties (Fig. 12).

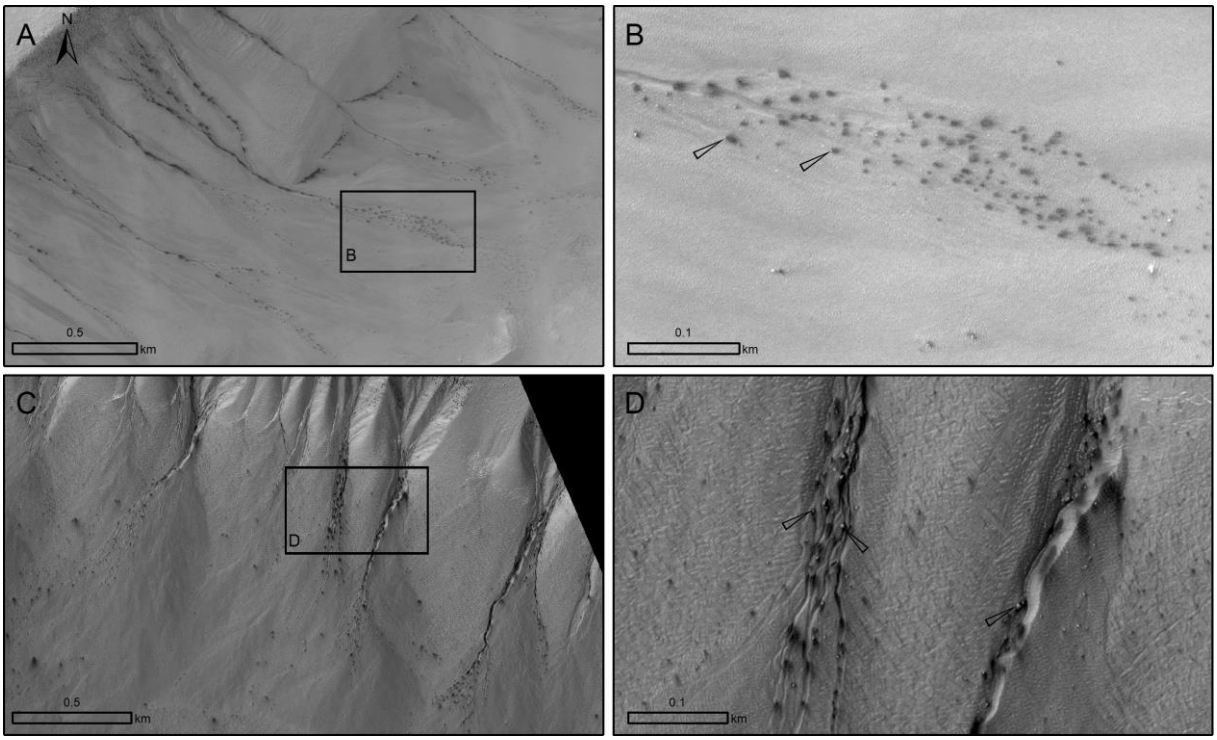

Fig. 11: Relation between gully morphologies (alcove, channel, apron) and dark spots/dark flows. A) A concentration of dark spots are present on gully-apron. HiRISE image ESP_046116_1115, Ls 159.9° (site n°1, area C: 68.3°S; 1.3°E). B) Zoom in on gully-apron on panel A, showing discontinuous channel segments and where arrows point to examples of visible boulders which make

this surface rougher. C) A concentration of dark spots and dark flows are visible inside the base of the gully alcove and channel. HiRISE image ESP_028618_1105, Ls 165.5° (site n°3: 69.5°S, 351.1°E). D) Zoom in on gully-alcove and channel on panel C, where arrows point to examples of visible boulders. Image credit: NASA/JPL/UofA. Note that each image was individually contrast-stretched.

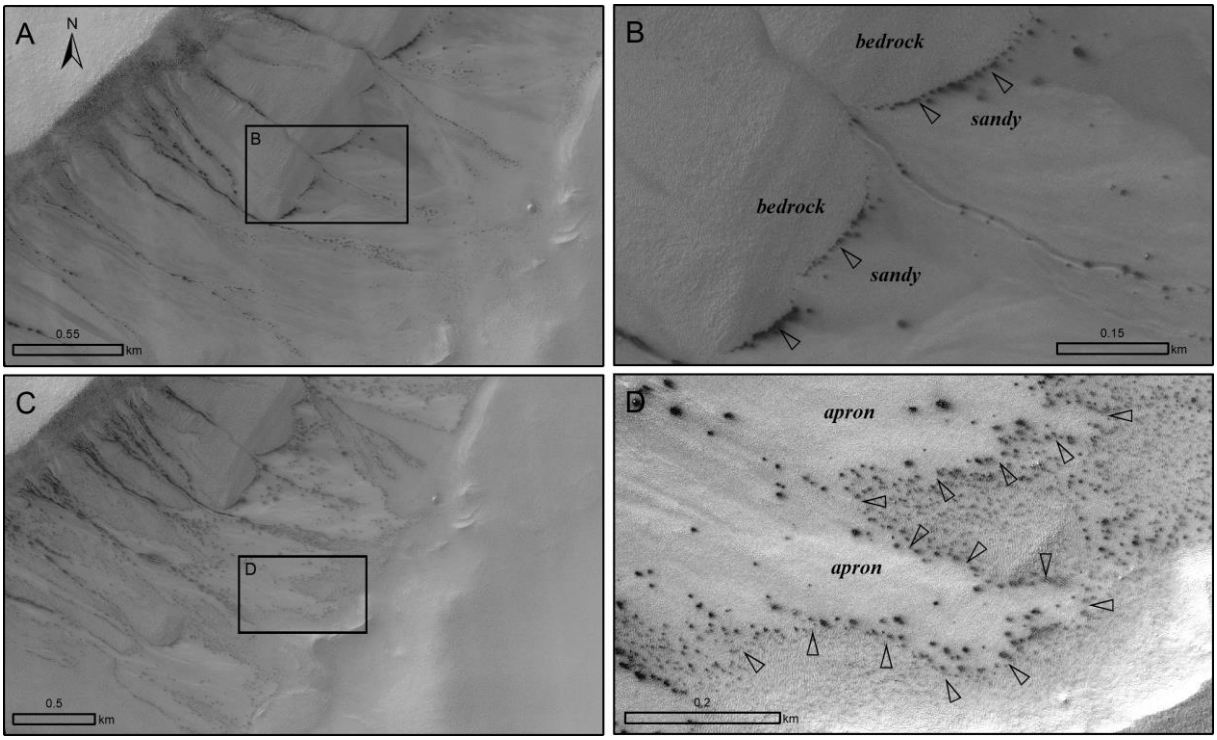

Fig. 12: Contrasts in substrate composition and presence of dark spots/dark flows (site n°1, area C: 68.3°S, 1.3°E). A) A concentration of dark spots/dark flows visible on a boundary between bedrock and a sandy substrate: HiRISE image ESP_046116_1115, Ls 159.9°. B) Zoom in on part of panel A with annotations and arrows pointing to aligned dark spots. C) The edge of gully aprons have a concentration of dark spots. HiRISE image ESP_028802_1115, Ls 173.3°. D) Annotated zoom in on panel C with the edge of the apron outlined by arrows. Image credit: NASA/JPL/UofA. Note that each image was individually contrast-stretched.

4. Discussion

The aim of this work is to better understand the relationship between gully activity and seasonal frost deposits in Sisyphi Cavi and to investigate if we can draw wider conclusions about this relationship for

gullies in general. We place our results into context with previous, related results from the literature. We discuss the significance of our findings regarding the sequence and timing of defrosting first, and the influence of gully activity on the presence of dark spots and dark flows second. Finally, we discuss the possible factors leading to gully activity and the possible effects of inhomogeneous frost distribution on gully morphology.

4.1. Frosted aprons as a precursor to gully activity?

Raack et al. (2015,2020) inventoried the gully activity of the Sisyphi Cavi area and showed that it occurs on area C between Ls 234° and Ls 252° (Raack et al., 2020) and in area D, between Ls 218° and 226° (Raack et al., 2015). Neither activity involved the erosion of material from the wall rock of the gully. This timing corresponds to a period when the alcoves have already begun to defrost, when frost is brighter and just before the surface becomes ice free (Fig. 5). For area D, we observe that a new and relatively dark deposit overlies an apron that is covered in brighter frost in both instances of documented gully activity (Fig. 14 B, C, Ls 226° and 227° respectively). In area C, the image acquired prior to the change documented by Raack et al. (2020) shows that the gully is completely covered in frost at Ls 235 (Fig. 14A). The following image, ESP_048107_1115 shown in Figure 3 of Raack et al. (2020), acquired 20° of solar longitude later, shows the new deposit. However, the apron could have been covered in frost when the activity occurred. Hence, it seems that a frost covered apron could be an important precursor to some gully activity – a possibility we expand on below.

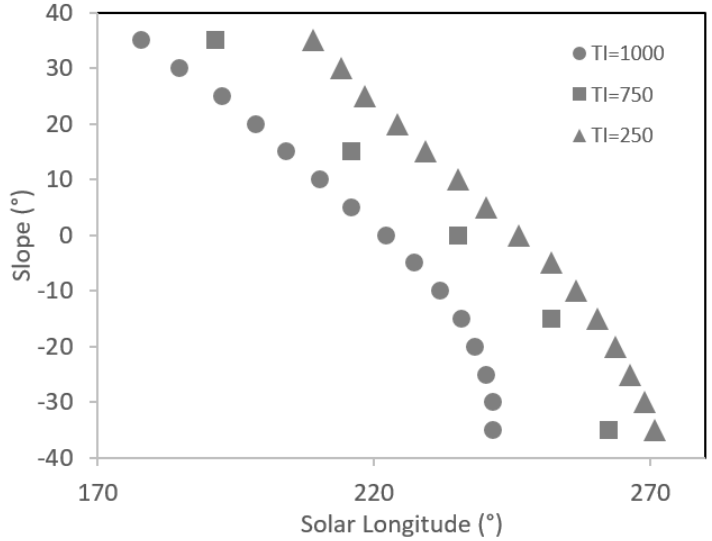

Fig. 13:Solar longitude of when defrosting of CO_2 occurs on slopes with different angles, where negative values represent pole-faing (south-facing) slopes and positive values equator-facing slopes. The results are obtained from 1D climate model simulations for different thermal inertias (TI).

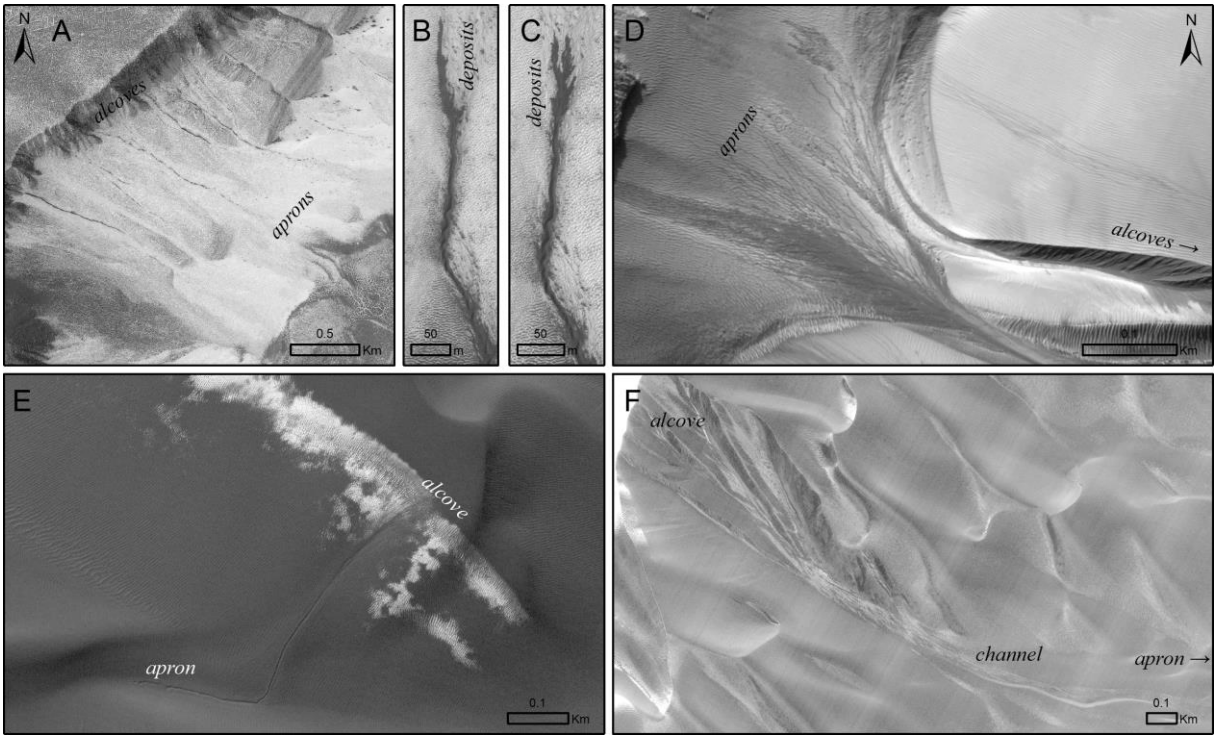

Fig. 14: Distribution of frost on gullies just before or just after gully activity: A) Site n°1, 68.5°S; 1.3°E, area C just before gully activity (MY33), HiRISE image: ESP_047751_1115, Ls 234.5° B) Site n°1, area D, just after gully activity, deposits are visible on top of the frosted apron, in MY31 (HiRISE image: ESP_029936_1115, Ls 225.6°) and C) shows the deposits for MY 29 (HiRISE image: PSP_003511_1115, Ls 226.7°) D) Gullies on the barchan dune of Kaiser crater (47.2°S; 19.5°E) just before gully activity, and the gully is entirely frosted, HiRISE image: ESP_018819_1330, Ls 126.8°, MY30; E) A linear gully on the Matara crater dunefield (49.5°S; 34.7°E) just before gully activity where only the alcove of gullies is frosted. The channel, and the terminal part of the gully are defrosted. HiRISE image: ESP_029038_1305, Ls 183.7°, MY31, F) Large sinuous gully on the Matara Crater dunefield (49.5°S; 34.7°E) just before gully activity, when the alcove, channel and the upper part of the apron are frosted, HiRISE image: ESP_036488_1300, Ls 128.1°, MY32. Image credit: NASA/JPL/UofA. Note that each image was individually contrast-stretched.

The fact that the gully alcoves defrost first in Sisyphi Cavi (Fig. 15; Supplementary Tables 3, 4 and 5) independent of orientation means that a factor other than solar insolation controls the onset of ice loss. The expected defrosting sequence starts at steep equator-facing slopes, then progresses towards shallower equator-facing slopes to flat surfaces, afterwards onto shallow pole-facing slopes and finally steep pole-facing slopes defrost. Making the assumption that the steepest slopes are found at the top of the hillslope consistent with the topographic measurements by Raack et al. (2020), this should result in the top of the pole-facing hillslope, where the alcoves are located, defrosting last. Instead we observe that it is the pole-facing aprons that are the last to defrost. We think this could be a key feature that could explain present-day activity in some martian gullies. From an informal survey of HiRISE images of typical mid-latitude gullies taken during the final stages of defrosting, we found several other examples where aprons remained frosted while the alcoves had already defrosted (Fig. 16). However, this does not seem to be a universal pattern in all gullies - for example, for linear gullies in the southern hemisphere (Pasquon et al., 2016) the channel and apron defrost before the alcove. The difference in behaviour is likely related to the substrate properties. In some gully systems, including those in Sisyphi Cavi the alcoves are comprised of rough rocky materials, whereas the aprons are presumably finer unconsolidated materials (as supported by studies of the thermal inertia of gully systems - Harrison et al., 2019; Khuller et al. 2021), so there are different materials on the same slope. Dune gullies in contrast have rather uniform substrate properties throughout, so follow the expected defrosting pattern (i.e. the steepest pole-facing slopes, defrost last).

In order to investigate this further we used surface temperature data from the 1D climate model runs presented in Conway et al. (2018). We extracted half-hourly surface temperature data for present day obliquity and position of perihelion for surface thermal inertia values of 250, 750 and 1000 Jm-2K-1s-0.5 (referred to as thermal inertia units or tiu) and slopes of 0-35° in the north- and south-facing orientations for 72°S. Thermal Emission Spectrometer (TES) data for the region suggests the average surface thermal inertia varies between 130 and 250 tiu. However, the TES footprint is >2 km, hence cannot capture local variations on the hillslopes which have a smaller spatial extent. Bedrock is expected to have values higher than 1200 tiu (Edwards et al., 2009), but is likely mixed with other materials in this area because it does not appear as continuous outcrop, hence we choose

intermediate values of 750 and 1000 tiu for illustrative purposes. From these data we extracted the solar longitude at which the surface temperature exceeds the condensation temperature of CO2 as shown in Fig. 13. From these data it can be seen for a constant thermal inertia the expected defrosting sequence starts at steep equator-facing slopes, then progresses towards shallower equator-facing slopes to flat surfaces, afterwards onto shallow pole-facing slopes and finally steep pole-facing slopes defrost last. Assuming aprons have a thermal inertia of 250 tiu and that alcoves are generally steeper than 30°, a pole-facing alcove with a thermal inertia of 750 tiu would defrost at the same time as a pole-facing apron. In contrast, a pole-facing alcove with a thermal inertia of 1000 tiu would defrost nearly 20° Ls before the pole-facing apron. Therefore, we infer the alcoves likely have a thermal inertia between these two extremes to explain the observations. The elevated thermal inertia of the gully alcoves with respect to gully fans could be due to a number of factors including, higher near-surface ice content, higher rockiness, larger grainsizes, or lower dustiness.

Other examples of gullies where mobilised material superposes a frosted apron exists. Dundas et al. (2015) observed dark flows over a frosted surface inside two gullies located at 37.4°S; 229°E; and in the northern hemisphere at 58.2°N and 89.7°E. On the dunes of Kaiser crater (47.2°S; 19.5°E), a gully shows an apron covered in frost just before the new gully deposits are observed (Fig. 14D; Dundas et al., 2012; Pasquon et al., 2019a). For the large sinuous gully on the Matara dunefield (49.5°S; 34.7°E), material from the alcove is mobilised over a frosted channel and apron (Fig. 14F; Dundas et al., 2012; Pasquon et al., 2019b). New gully deposits are usually not first imaged/detected during the defrosting season, and therefore we do not know if they were emplaced while the aprons were covered in frost. However, other observations suggest that the activity occurs primarily during the defrosting season (Dundas et al. 2019), meaning it is not unreasonable to assume that the deposits are commonly mobilised over a frosted surface. The only notable exception is for linear gullies, where frost is still present in the alcoves (generally) when activity occurs (Fig. 14E; Dinwiddie and Titus 2021; Jouannic et al., 2012; 2019; Pasquon et al., 2016). We note that for gullies on sand dunes, discrete scars in the sandy alcoves are often associated with activity (e.g., Pasquon et al., 2019b), yet in gullies with bedrock alcoves, none of the observed activities had detectable erosion of the wall rock in the alcoves (Dundas et al. 2012; 2019). This lack of erosion, could mean that CO_2 related processes are not responsible for the formation

of the whole gully landform or could simply reflect that the temporal baseline of observation is not long enough to detect erosion into these presumably more durable materials (Levin et al. 2022).

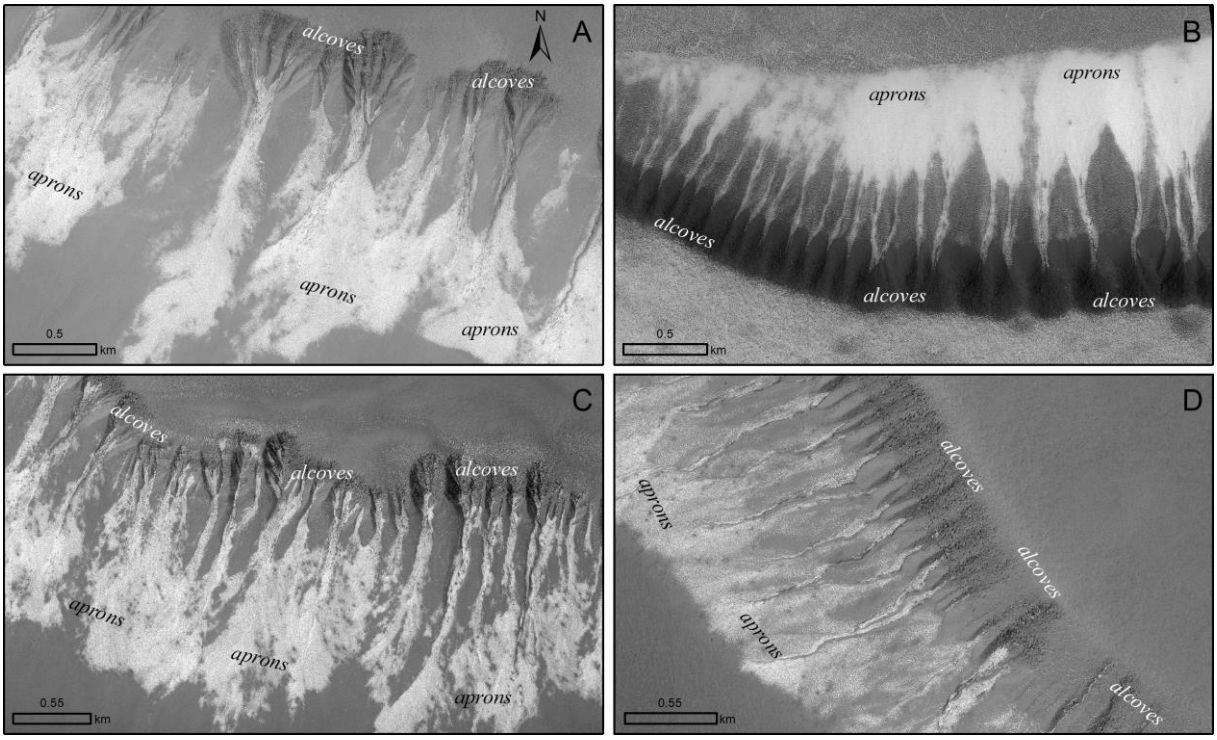

Fig. 15: Examples with various slope orientations from Sisyphi Cavi where the aprons remain frosted while the surrounding terrain is defrosted . A) HiRISE image: ESP_039286_1105, Ls 251.9°, (69.4°S and 347°E); B) HiRISE image: ESP_012530_1090, Ls 236.7°, (70.9°S and 1.3°E); C) HiRISE image: ESP_039325_1090, Ls 253.8°, (70.9°S and 1.2°E); D) HiRISE image: ESP_057021_1090, Ls 256.9°, (70.7°S and 4.3°E). Image credit: NASA/JPL/UofA. Note that each image was individually contrast-stretched.

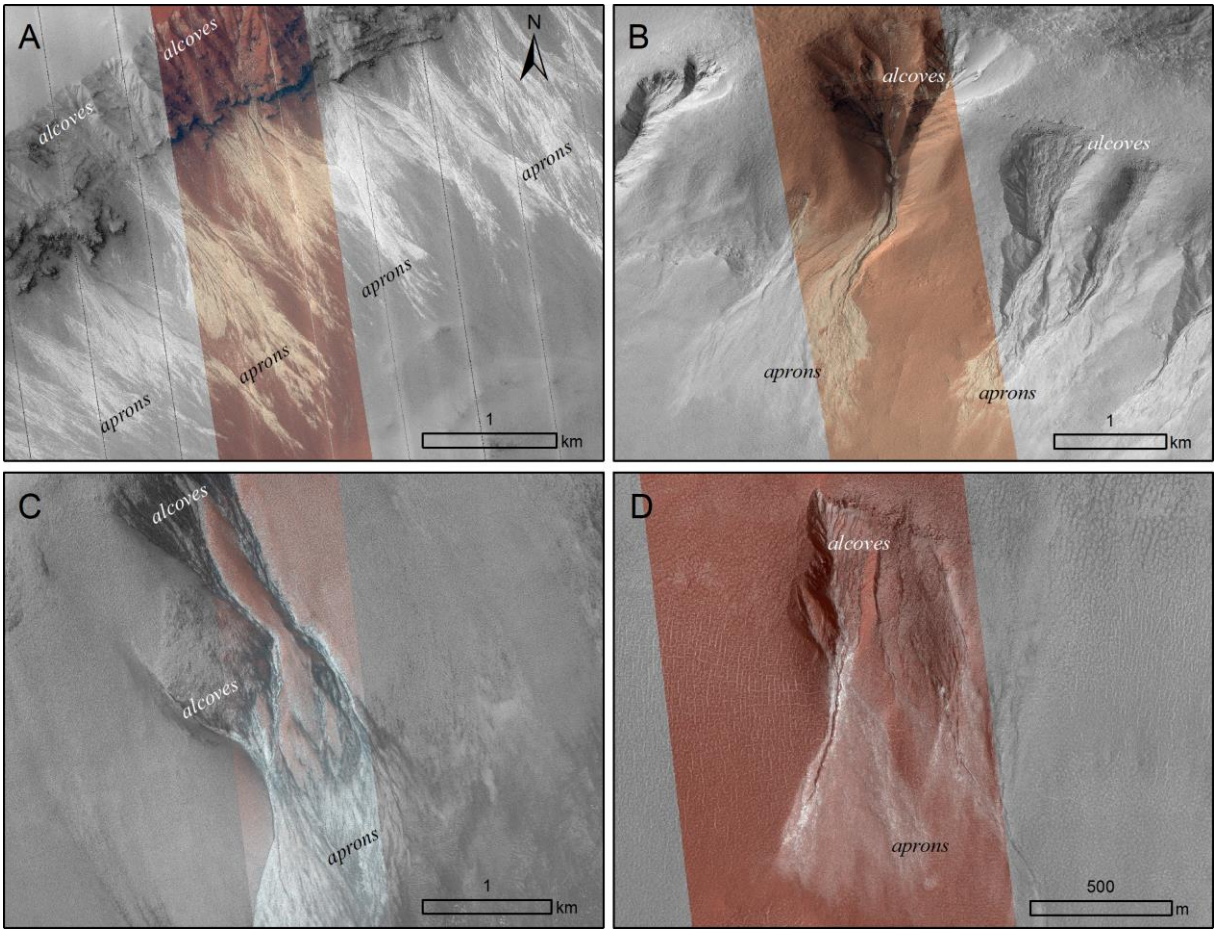

Fig. 16: Examples of gullies in the southern hemisphere on Mars in which the alcoves defrost before the channel and the apron: A) HiRISE image: ESP_056433_1160, Ls 227.9°, (63.5°S; 212.1°E), B) HiRISE image: ESP_011400_1275, Ls 183.4°, (52.2°S; 246.9°E), C) HiRISE image: ESP_011477_1275, Ls 186.9°, (52°S; 304.9°E), D) HiRISE image: ESP_029421_1250, Ls 201.1°, (54.6°S; 17.5°E). Image credit: NASA/JPL/UofA. Note that each image was individually contrast-stretched.

4.2 Dark spots and flows as an indicator of recent gully activity

We observe that boulders, rough surfaces inside channels and on the aprons of gullies, and contrasts in surface type (e.g. the edge of a dune field) are preferential locations for dark spots (and sometimes dark flows) (Figs. 8-10). Boulders have been noted previously as initiation points for dark spots and fans (Thomas et al. 2010). In this context, our observed strong spatial correlation between the appearance of dark spots/flows and surface roughness could be explained by the following hypotheses:

1) Surface roughness, in particular non-homogenous thermal inertia, should cause spatial heterogeneities in the temperature field of the substrate and thus also in the sublimation of the

ice layer. More gas may be produced on the sun-facing side of a boulder, for example, causing preferential pressure build-up at that location, as warmer surfaces defrost faster.

2) Surface roughness (e.g. boulders or levees), in particular gradients in normal stresses caused by variable overburden thicknesses or densities, could cause bending moments and mechanical weakness in the overlying CO_2 ice slab. This would pre-condition that location for failure when the gas pressure builds up.

3) Both of the aforementioned factors could be at play.

The fact that surface roughness promotes more numerous dark spots and flows can be combined with the fact that recently active gullies tend to have rougher surfaces (Dundas et al. 2019). For this reason they could assist in detecting recently active sites without the need for repeat imaging. Repeat images could then be targeted at this zone as active sites are often repeatedly active.

We now interrogate what role is played by the dark/spots flows in gully activity. Surface modification events in gullies in Sisyphi Cavi are less frequent compared to gullies on sand dunes or sandy surfaces on Mars, which are generally active annually (e.g. Dundas et al., 2012; 2015; 2020; Pasquon et al., 2019b). Activity of gullies on dunes is accompanied by a similar sequence of defrosting patterns to those we report for Sisyphi Cavi, including the appearance of dark spots followed by their transformation into dark flows as the surface warms (Jouannic et al., 2012; 2019). The activity of gullies occurs generally during the final stages of defrosting. The frequency of activity on Sisyphi Cavi is comparable and consistent with gullies on non-sandy surfaces e.g., crater walls (Dundas et al., 2019), but in contrast observations of dark spots and flows are rather rare in these systems. For both areas studied in detail in Sisyphi Cavi (areas C and D at 68°S; 1.3°E) only 2 out of 33 gullies are active between MY28 and MY35 (Raack et al., 2015; 2020). One gully on area C is active and just once over a period of 8 MY. Only one gully is active in area D in MYs 29 and 31. So, material movement in these two areas seems to be relatively sparse. The disconnect between the widespread presence and annual occurrence of dark spots and dark flows and the low spatial and temporal frequency of activity in gullies might suggests that dark spots and dark flows are not a primary agent in triggering gully activity. .

5. Conclusion

In this paper we explored the process of defrosting in gully-incised slopes in Sisyphi Cavi. We explored the sequence, timing, and duration of events that occur during seasonal defrost, and their connection to gully and dark spot/dark flow activity. We find that the general timing and characteristics of the seasonal defrosting patterns in Sisyphi Cavi are very consistent from year to year, and similar to the general trend observed at a global scale for the seasonal frost deposits. Our observations show that the absolute timing of the different stages of the defrosting sequence is influenced by the overall orientation of the host hillslope, with equator-facing slopes generally defrosting earlier than the pole-facing ones. Gully alcoves defrost first before channels and aprons and independently of orientation. This is unexpected because based on incoming solar radiation the defrosting should progress from the top of equator-facing slope down towards the flat floor and up the pole-facing slope, terminating at the top. We argue that this could be due to the dominant effect of contrasting substrates between alcove (rocky materials) and aprons (finer unconsolidated materials) over the role of solar insolation and orientation during the early stages of defrost. We also observe that gullies defrost later than their surrounding terrain, with some frost patches remaining in the interior of channels and alcoves at the end of defrosting, likely due to shadowing.

We also find that dark spots and flows concentrate in areas of increased surface roughness. This suggests that gully activity, which creates surface roughness via contrasts in material types, deposition of boulders levees and lobes and erosion to form braiding, can facilitate the appearance of dark spots and dark flows over the affected area the following winter. We therefore infer that dark spots and dark flows could be used to help to detect recently active gullies on Mars without repeat imaging, but they themselves are not a precursor to gully activity.

Finally, we note that a prerequisite for gully activity in Sisyphi Cavi is a frosted apron surface. We show that such a configuration is found in gully-sites elsewhere on Mars, raising the possibility that this is a common precursor for gully activity, where seasonal frost is present. We note that this type of activity is not associated with detectable erosion of the wall rock in the alcoves, which could mean erosion by CO_2 related process is too small to be detectable in these durable materials or that another process is responsible for the initial formation of gullies.

6. Acknowledgments

We'd like to thank Ginny Gulick and Aditya Khuller whose detailed and helpful reviews increased the quality of the manuscript. The HiRISE data used in this study can be accessed from the Planetary Data System https://pds-imaging.jpl.nasa.gov/volumes/mro.html or at or the PI website at https://www.uahirise.org/ and the CaSSIS data can be accessed via the PSA at https://archives.esac.esa.int or the PI website at https://observations.cassis.unibe.ch/. The authors are grateful for the financial support from Région Pays de la Loire, project étoiles montantes METAFLOWS (convention N° 2019-14294) and also the financial support of CNES in support of their CaSSIS work. The authors thank the spacecraft and instrument engineering teams for the successful completion and operation of CaSSIS. CaSSIS is a project of the University of Bern funded through the Swiss Space Office via ESA's PRODEX programme. The instrument hardware development was also supported by the Italian Space Agency (ASI) (ASI-INAF agreement no. I/018/12/0), INAF/ Astronomical Observatory of Padova, and the Space Research Center (CBK) in Warsaw. Support from SGF (Budapest), the University of Arizona (LPL) and NASA are also gratefully acknowledged. Operations support from the UK Space Agency under grant ST/R003025/1 is also acknowledged. SRL is supported by UK Space Agency grants ST/W002949/1, ST/V005332/1, and ST/T002913/1. Thanks goes to Valentin Bickel and Candy Hansen for informal comments that improved the manuscript.

7. References cited

Andrieu, F., Schmidt, F., Douté, S., Chassefière, E., 2018. Ice state evolution during spring in Richardson crater, Mars. Icarus 315, 158–173. https://doi.org/10.1016/j.icarus.2018.06.019

Auld, K. S., and J. C. Dixon (2016), A classification of martian gullies from HiRISE imagery, Planetary and Space Science, 131, 88–101.

Balme, M., N. Mangold, D. Baratoux, F. Costard, M. Gosselin, P. Masson, P. Pinet, and G. Neukum (2006), Orientation and distribution of recent gullies in the southern hemisphere of Mars: observations

from High Resolution Stereo Camera/Mars Express (HRSC/MEX) and Mars Orbiter Camera/Mars Global Surveyor (MOC/MGS) data, Journal of Geophysical Research: Planets, 111(E5).

Brown, A.J., Calvin, W.M., McGuire, P.C., Murchie, S.L., 2010. Compact Reconnaissance Imaging Spectrometer for Mars (CRISM) south polar mapping: First Mars year of observations. J. Geophys. Res. 115, E00D13.

Calvin, W.M., Cantor, B.A., James, P.B., 2017. Interannual and seasonal changes in the south seasonal polar cap of Mars: Observations from MY 28-31 using MARCI. Icarus 292, 144–153. https://doi.org/10.1016/j.icarus.2017.01.010

Cedillo-Flores, Y., A. H. Treiman, J. Lasue, and S. M. Clifford (2011), CO_2 gas fluidization in the initiation and formation of Martian polar gullies, Geophysical Research Letters, 38(21).

Christensen, P. R. (2003), Formation of recent Martian gullies through melting of extensive water-rich snow deposits, Nature, 422(6927), 45.

Conway, S. J., M. R. Balme, J. B. Murray, M. C. Towner, C. H. Okubo, and P. M. Grindrod (2011), The indication of Martian gully formation processes by slope–area analysis, Geological Society, London, Special publications, 356(1), 171–201.

Conway, S. J., and M. R. Balme (2016), A novel topographic parameterization scheme indicates that Martian gullies display the signature of liquid water, Earth and Planetary Science Letters, 454, 36–45.

Conway, S.J., Harrison, T.N., Lewis, S.R., 2018. Chapter 3: Martian gullies and their connection with the martian climate, in: Soare, R.J., Conway, Susan J., Clifford, S.M. (Eds.), Dynamic Mars: Recent and Current Landscape Evolution of the Red Planet. Elsevier.

Conway, S. J., T. N. Harrison, R. J. Soare, A. W. Britton and L. J. Steele (2019a), New slope-normalized global density and orientation maps for Mars, Geological Society, London, Special Publications, 467, 187-197, 27 November 2017.

Costard, F., F. Forget, N. Mangold, and J. Peulvast (2002), Formation of recent Martian debris flows by melting of near-surface ground ice at high obliquity, Science, 295(5552), 110–113.

Di Achille, G., S. Silvestro, and G. Ori (2008), Defrosting processes on dark dunes: New insights from HiRISE images at Noachis and Aonia Terrae, Mars, in Planetary Dunes Workshop, vol. 1403, pp. 27–28.

Diniega, S., S. Byrne, N. T. Bridges, C. M. Dundas, and A. S. McEwen (2010), Seasonality of present-day Martian dune-gully activity, Geology, 38(11), 1047–1050.

Diniega, S., C. Hansen, J. McElwaine, C. Hugenholtz, C. Dundas, A. McEwen, and C. Bourke (2013), A new dry hypothesis for the formation of martian linear gullies, Icarus, 225, 526–537.

Dickson, J. L., J. W. Head, and M. Kreslavsky (2007), Martian gullies in the southern midlatitudes of Mars: Evidence for climate-controlled formation of young fluvial features based upon local and global topography, Icarus, 188(2), 315–323.

Dickson, J. L., J. W. Head, and C. I. Fassett (2012), Patterns of accumulation and flow of ice in the mid-latitudes of Mars during the Amazonian, Icarus, 219(2), 723–732.

Dinwiddie, C.L., Titus, T.N., 2021. Airborne Dust Plumes Lofted by Dislodged Ice Blocks at Russell Crater, Mars. Geophysical Research Letters 48. https://doi.org/10.1029/2020GL091920

Dundas, C. M., S. Diniega, C. J. Hansen, S. Byrne, and A. S. McEwen (2012), Seasonal activity and morphological changes in Martian gullies, Icarus, 220(1), 124–143.

Dundas, C. M., A. S. McEwen, S. Diniega, S. Byrne, and S. Martinez-Alonso (2010), New and recent gully activity on Mars as seen by HiRISE, Geophysical Research Letters, 37(7).

Dundas, C. M., S. Diniega, and A. S. McEwen (2015), Long-term monitoring of Martian gully formation and evolution with MRO/HiRISE, Icarus, 251, 244–263.

Dundas, C. M., A. S. McEwen, S. Diniega, C. J. Hansen, S. Byrne, and J. N. McElwaine. 2019, The formation of gullies on Mars today, Geological Society, London, Special Publications, 467, SP467–5.

Gaidos, E. J. (2001), Cryovolcanism and the recent flow of liquid water on Mars, Icarus, 153(1), 218–223.

Edwards, C.S., Bandfield, J.L., Christensen, P.R., Fergason, R.L., 2009. Global distribution of bedrock exposures on Mars using THEMIS high-resolution thermal inertia. J. Geophys. Res. 114, E11001. https://doi.org/10.1029/2009JE003363

Gardin, E., P. Allemand, C. Quantin, and P. Thollot (2010), Defrosting, dark flow features, and dune activity on Mars: Example in Russell crater, Journal of Geophysical Research: Planets, 115(E6).

Hansen, C., et al. (2011), Seasonal erosion and restoration of Mars northern polar dunes, Science, 331(6017), 575–578.

Harrison, T. N., G. R. Osinski, L. L. Tornabene, and E. Jones (2015), Global documentation of gullies with the Mars Reconnaissance Orbiter Context Camera and implications for their formation, Icarus, 252, 236–254.

Harrison, T. N., L. L. Tornabene, G. R., Osinski, and S. J. Conway (2019), Thermal inertia variations from gully and mass-wasting activity in Gasa crater, Mars Geological Society, London, Special Publications, 467, 1999-210.

Hartmann, W. K. (2001), Martian seeps and their relation to youthful geothermal activity, Space Science Reviews, 96(1), 405–410.

Hauber, E., et al. (2011), Landscape evolution in Martian mid-latitude regions: insights from analogous periglacial landforms in Svalbard, Geological Society, London, Special Publications, 356(1), 111–131.

Heldmann, J. L., and M. T. Mellon (2004), Observations of Martian gullies and constraints on potential formation mechanisms, Icarus, 168(2), 285–304.

Heldmann, J. L., O. B. Toon, W. H. Pollard, M. T. Mellon, J. Pitlick, C. P. McKay, and D. T. Andersen (2005), Formation of Martian gullies by the action of liquid water flowing under current Martian environmental conditions, Journal of Geophysical Research: Planets, 110(E5).

Hoffman, N. (2002), Active polar gullies on Mars and the role of carbon dioxide, Astrobiology, 2(3), 313–323.

Hugenholtz, C. H. (2008), Frosted granular flow: A new hypothesis for mass wasting in Martian gullies, Icarus, 197(1), 65–72.

Ishii, T., and S. Sasaki (2004), Formation of recent Martian gullies by avalanches of CO_2 frost, in Lunar and Planetary Science Conference, vol. 35.

Jouannic, G., J. Gargani, F. Costard, G. G. Ori, C. Marmo, F. Schmidt, and A. Lucas (2012), Morphological and mechanical characterization of gullies in a periglacial environment: The case of the Russell crater dune (Mars), Planetary and Space Science, 71(1), 38–54.

Jouannic, G., J. Gargani, S. J. Conway, F. Costard, M. R. Balme, M. R. Patel, M. Massé, C. Marmo, V. Jomelli, and G.G. Ori, (2015), Laboratory simulation of debris flows over sand dunes: Insights into gully-formation (Mars), Geomorphology, 231, 101–115.

Jouannic, G., S. J. Conway, J. Gargani, F. Costard, M. Massé, O. Bourgeois, J. Carter, F., Schmidt, C. Marmo, G. G. Ori, M. Nachon, and K. Pasquon, (2019), Morphological characterisation of landsforms produced by springtime seasonal activity on Russel crater megadune, Mars, Geological Society, London, Special Publications, 467. doi:10.1144/SP467.16.

Kereszturi, A., D. Möhlmann, S. Berczi, T. Ganti, A. Kuti, A. Sik, and A. Horvath (2009), Recent rheologic processes on dark polar dunes of Mars: Driven by interfacial water ?, Icarus, 201(2), 492–503.

Kereszturi, A., D. Möhlmann, S. Berczi, T. Ganti, A. Horvath, A. Kuti, A. Sik, and E. Szathmary (2010), Indications of brine related local seepage phenomena on the northern hemisphere of Mars, Icarus, 207(1), 149–164.

Kereszturi, A., D. Möhlmann, S. Berczi, A. Horvath, A. Sik, and E. Szathmary (2011), Possible role of brines in the darkening and flow-like features on the Martian polar dunes based on HiRISE images, Planetary and Space Science, 59(13), 1413–1427.

Khuller, A., Christensen, P., 2021. Evidence of Exposed Dusty Water Ice within Martian Gullies. J Geophys Res Planets 126. https://doi.org/10.1029/2020JE006539

Khuller, A.R., Christensen, P.R., Harrison, T.N., Diniega, S., 2021. The Distribution of Frosts on Mars: Links to Present- Day Gully Activity. J Geophys Res Planets. https://doi.org/10.1029/2020JE006577

Kieffer, H. H. (2000), Annual punctuated CO_2 slab-ice and jets on Mars, in Second International Conference on Mars Polar Science and Exploration, p. 93.

Kieffer, H. H. (2007), Cold jets in the Martian polar caps, Journal of Geophysical Research: Planets, 112(E8).

Kieffer, H. H., P. R. Christensen, and T. N. Titus (2006), CO_2 jets formed by sublimation beneath translucent slab ice in Mars seasonal south polar ice cap, Nature, 442(7104), 793.

Knauth, L. P., and D. M. Burt (2002), Eutectic brines on Mars: Origin and possible relation to young seepage features, Icarus, 158(1), 267–271.

Lange, L., Piqueux, S., Edwards, C.S., (2022), Gardening of the Martian Regolith by Diurnal CO_2 Frost and the Formation of Slope Streaks. JGR Planets 127. https://doi.org/10.1029/2021JE006988

Langevin, Y., Bibring, J.-P., Montmessin, F., Forget, F., Vincendon, M., Douté, S., Poulet, F., Gondet, B. (2007), Observations of the south seasonal cap of Mars during recession in 2004-2006 by the OMEGA visible/near-infrared imaging spectrometer on board Mars Express J. Geophys. Res. 112. https://doi.org/10.1029/2006JE002841

Lee, P., C. S. Cockell, M. M. Marinova, C. P. McKay, and J. W. Rice Jr (2001), Snow and ice melt flow features on Devon Island, Nunavut, Arctic Canada as possible analogs for recent slope flow features on Mars.

Levin, J.N., Dickson, J.L., Lamb, M.P., 2022. Evaluating the Role of Volatiles in Bedrock Chute Formation on the Moon and Mars. Icarus 373, 114774. https://doi.org/10.1016/j.icarus.2021.114774

Malin, M. (1998), Mars Orbiter Camera: The first year, in Bulletin of the American Astronomical Society, vol. 30, p. 1020.

Malin, M. C., and K. S. Edgett (2000), Evidence for recent groundwater seepage and surface runoff on Mars, Science, 288(5475), 2330–2335.

Malin, M. C., K. S. Edgett, L. V. Posiolova, S. M. McColley, and E. Z. N. Dobrea (2006), Present-day impact cratering rate and contemporary gully activity on Mars, science, 314(5805), 1573–1577.

Mangold, N., F. Costard, and F. Forget (2003), Debris flows over sand dunes on Mars: Evidence for liquid water, Journal of Geophysical Research: Planets, 108(E4).

Mangold, N., A. Mangeney, V. Migeon, V. Ansan, A. Lucas, D. Baratoux, and F. Bouchut (2010), Sinuous gullies on Mars: Frequency, distribution, and implications for flow properties, Journal of Geophysical Research: Planets, 115(E11).

Massé, M., S. J. Conway, J. Gargani, M. R. Patel, K. Pasquon, A. McEwen, S. Carpy, V. Chevrier, M.R., Balme, L. Ojha, M. Vincendon, F. Poulet, F. Costard and G. Jouannic, (2016), Transport processes induced by metastable boiling water under Martian surface conditions, Nature Geoscience, 9(6), 425–428.

McEwen, A. S., et al. (2007), Mars Reconnaissance Orbiter's High Resolution Imaging Science Experiment (HiRISE), Journal of Geophysical Research: Planets, 112(E5).

Mellon, M. T., and R. J. Phillips (2001), Recent gullies on Mars and the source of liquid water, Journal of Geophysical Research: Planets, 106(E10), 23,165–23,179.

Miyamoto, H., J. M. Dohm, V. R. Baker, R. A. Beyer, and M. Bourke (2004), Dynamics of unusual debris flows on Martian sand dunes, Geophysical Research Letters, 31(13).

Möhlmann, D., and A. Kereszturi (2010), Viscous liquid film flow on dune slopes of Mars, Icarus, 207(2), 654–658.

Musselwhite, D. S., T. D. Swindle, and J. I. Lunine (2001), Liquid CO_2 breakout and the formation of recent small gullies on Mars, Geophysical Research Letters, 28(7), 1283–1285.

Ojha, L., M. B. Wilhelm, S. L. Murchie, A. S. McEwen, J. J. Wray, J. Hanley, M. Massé, and M. Chojnacki (2015), Spectral evidence for hydrated salts in Recurring Slope Lineae on Mars, Nature Geoscience, 8(11), 829–832.

Pilorget, C., and F. Forget (2016), Formation of gullies on Mars by debris flows triggered by CO_2 sublimation, Nature Geoscience, 9(1), 65–69.

Pasquon, K., J. Gargani, M. Massé, and S. J. Conway (2016), Present-day formation and seasonal evolution of linear dune gullies on Mars, Icarus, 274, 195–210.

Pasquon, K., J. Gargani, M. Nachon, S. J. Conway, M. Massé, G. Jouannic, M. R. Balme, F. Costard, and M. Vincendon, (2019a), Are the different gully morphologies due to different formation processes on the Kaiser due field?, Geological Society, London, Special Publications, 467. doi.org/10.1144/SP467.13.

Pasquon, K., J. Gargani, M. Massé, M. Vincendon, S. J. Conway, A. Séjourné, V. Jomelli, M. R. Balme, S. Lopez, and A. Guimpier, (2019b), Present-day development of gully-channel sinuosity by carbon dioxide gas supported flows on Mars, Icarus 329, 293-313.

Piqueux, S., Kleinböhl, A., Hayne, P.O., Heavens, N.G., Kass, D.M., McCleese, D.J., Schofield, J.T., Shirley, J.H., 2016. Discovery of a widespread low-latitude diurnal CO 2 frost cycle on Mars: Low-Latitude CO 2 Frost on Mars. Journal of Geophysical Research: Planets. https://doi.org/10.1002/2016JE005034

Piqueux, S., Kleinböhl, A., Hayne, P.O., Kass, D.M., Schofield, J.T., McCleese, D.J., 2015. Variability of the martian seasonal CO2 cap extent over eight Mars Years. Icarus 251, 164–180. https://doi.org/10.1016/j.icarus.2014.10.045

Piqueux, S., and P. R. Christensen (2008), North and south subice gas flow and venting of the seasonal caps of Mars: A major geomorphological agent, Journal of Geophysical Research : Planets, 113(E6).

Piqueux, S., S. Byrne, and M. I. Richardson (2003), Sublimation of Mars's southern seasonal CO_2 ice cap and the formation of spiders, Journal of Geophysical Research: Planets, 108(E8).

Pommerol, A., Appéré, T., Portyankina, G., Aye, K.-M., Thomas, N., Hansen, C.J., 2013. Observations of the northern seasonal polar cap on Mars III: CRISM/HiRISE observations of spring sublimation. Icarus 225, 911–922. https://doi.org/10.1016/j.icarus.2012.08.039

Raack, J., D. Reiss, T. Appéré, M. Vincendon, O. Ruesch, and H. Hiesinger, (2015), Present-day seasonal gully activity in a south polar pit (Sisyphi Cavi) on Mars, Icarus, 251, 226-243.

Raack, J., S. J. Conway, T. Heyer, V. T. Bickel, M. Philippe, H. Hiesinger, A. Johnsson, and M. Massé, (2020), Present-day gully activity in Sisyphi Cavi, Mars – flow-like features and block movements, Icarus, 350, 113899.

Reiss, D., G. Erkeling, K. Bauch, and H. Hiesinger (2010), Evidence for present day gully activity on the Russell crater dune field, Mars, Geophysical Research Letters, 37(6).

Reiss, D., and R. Jaumann (2003), Recent debris flows on Mars: Seasonal observations of the Russell crater dune field, Geophysical Research Letters, 30(6).

Schorghofer, N., and K. S. Edgett (2006), Seasonal surface frost at low latitudes on Mars, Icarus, 180(2), 321–334.

Shinbrot, T., N.-H. Duong, L. Kwan, and M. Alvarez (2004), Dry granular flows can generate surface features resembling those seen in Martian gullies, Proceedings of the National Academy of Sciences of the United States of America, 101(23), 8542–8546.

Singh, D., Flanner, M.G., 2016. An improved carbon dioxide snow spectral albedo model: Application to Martian conditions: CARBON DIOXIDE SNOW ALBEDO MODEL. J. Geophys. Res. Planets 121, 2037–2054. https://doi.org/10.1002/2016JE005040

Smith, D. E., M. T. Zuber, and G. A. Neumann (2001), Seasonal variations of snow depth on Mars, Science, 294(5549), 2141–2146.

Stewart, S. T., and F., Nimmo, (2002), Surface runoff features on Mars: testing the carbon dioxide formation hypothesis, Journal of Geophysical Research: Planets, 107 (E9).

Tanaka, K. L., and D. H. Scott, (1987), Geologic map of the polar regions of Mars, In :USGS Map I-1802C

Thomas, N., Cremonese, G., Ziethe, R., Gerber, M., Brändli, M., Bruno, G., Erismann, M., Gambicorti, L., Gerber, T., Ghose, K., Gruber, M., Gubler, P., Mischler, H., Jost, J., Piazza, D., Pommerol, A., Rieder, M., Roloff, V., Servonet, A., Trottmann, W., Uthaicharoenpong, T., Zimmermann, C., Vernani, D., Johnson, M., Pelò, E., Weigel, T., Viertl, J., De Roux, N., Lochmatter, P., Sutter, G., Casciello, A., Hausner, T., Ficai Veltroni, I., Da Deppo, V., Orleanski, P., Nowosielski, W., Zawistowski, T., Szalai, S., Sodor, B., Tulyakov, S., Troznai, G., Banaskiewicz, M., Bridges, J.C., Byrne, S., Debei, S., El-Maarry, M.R., Hauber, E., Hansen, C.J., Ivanov, A., Keszthelyi, L., Kirk, R., Kuzmin, R., Mangold, N., Marinangeli, L., Markiewicz, W.J., Massironi, M., McEwen, A.S., Okubo, C., Tornabene, L.L., Wajer, P., Wray, J.J. (2017), The Colour and Stereo Surface Imaging System (CaSSIS) for the ExoMars Trace Gas Orbiter. Space Science Reviews 212, 1897–1944. https://doi.org/10.1007/s11214-017-0421-1

Thomas, N., Hansen, C.J., Portyankina, G., Russell, P.S. (2010), HiRISE observations of gas sublimation-driven activity in Mars' southern polar regions: II. Surficial deposits and their origins. Icarus 205, 296–310. https://doi.org/10.1016/j.icarus.2009.05.030

Treiman, A. H. (2003), Geologic settings of Martian gullies: Implications for their origins, Journal of Geophysical Research: Planets, 108(E4).

Védie, E., F. Costard, M. Font, and J. Lagarde (2008), Laboratory simulations of Martian gullies on sand dunes, Geophysical Research Letters, 35(21).

Vincendon, M. (2015), Identification of Mars gully activity types associated with ice composition, Journal of Geophysical Research: Planets, 120(11), 1859–1879.

Vincendon, M., F. Forget, and J. Mustard (2010), Water ice at low to midlatitudes on Mars, Journal of Geophysical Research: Planets, 115(E10).

Williams, K., O. Toon, J. Heldmann, and M. Mellon (2009), Ancient melting of mid-latitude snowpacks on Mars as a water source for gullies, Icarus, 200(2), 418–425.

Supplementary material

Supplementary Table S1: CaSSIS and HiRISE images used for this study for the 3 sites 1) 68.5°S and 1.3°E (Fig. 1B), 2) 70.92°S and 1.2°E (Fig. 1C) and 3) 69.4°S and 347°E (Fig. 1D). x = image covers the area/site indicated. Ls = Solar Longitude. MY= martian year.

Site 1	CaSSIS image	Ls	Site 1
MY35	MY35_011819_257_0	240.43°	X
	MY35_011760_288_0	237.38°	X
	MY35_011300_286_0	213.89°	X
MY34	MY34_004583_256_0	299.49°	X
	MY34_003815_284_0	260.56°	X
	MY34_003616_284_1	250.23°	X
	MY34_003616_284_2	250.23°	X
	MY34_003464_256_1	242.34°	X
	MY34_003464_256_2	242.34°	X
	MY34_002124_284_2	176.28°	X
	MY34_002124_284_1	176.23°	X
Site 3			
MY35	MY35_011748_286_0	236.76°	X
MY34	MY34_003974_259_0	268.78°	X
	MY34_002122_259_2	176.18°	X

Site 1	HiRISE image	Ls	Area A	Area B	Area C	Area D
MY35	ESP_065896_1115	259.8°		x		
	ESP_064643_1115	199°	x	x	x	x
	ESP_064221_1115	180°	x	x	x	x
	ESP_063865_1115	164.7°	x	x	x	x
MY34	ESP_057707_1115	290.3°		x		
	ESP_056731_1115	242.6°	x	x	x	x
	ESP_056520_1115	232.2°	x	x	x	x
	ESP_056177_1115	215.6°	x	x	x	x
	ESP_055900_1115	202.5°	x	x	x	x
	ESP_055689_1115	192.7°	x	x	x	x
	ESP_055478_1115	183.3°	x	x	x	x
MY33	ESP_049109_1115	300.6°	x	x	x	x
	ESP_048107_1115	252.1°		x		
	ESP_047751_1115	234.5°	x	x	x	x
	ESP_047593_1115	226.8°	x	x	x	x
	ESP_047461_1115	220.4°	x	x	x	x
	ESP_047250_1115	210.3°	x	x	x	x
	ESP_047039_1115	200.4°	x	x	x	x
	ESP_046538_1115	177.8°	x	x	x	x

	ESP_046472_1115	174.9°	x	x	x	x
	ESP_046116_1115	159.9°	x	x	x	x
MY32	ESP_039615_1115	268.1°	x	x	x	x
	ESP_039114_1115	243.4°	x	x	x	x
	ESP_038283_1115	203.2°	x	x	x	x
	ESP_038151_1115	197.1°	x	x	x	x
	ESP_037729_1115	178.1°	x	x	x	x
	ESP_037452_1115	166.3°	x	x	x	x
	ESP_037307_1115	160.2°	x	x	x	x
MY31	ESP_030701_1115	263.3°	x	x	x	x
	ESP_030503_1115	253.5°	x	x	x	x
	ESP_030503_1115	253.5°	x	x	x	x
	ESP_030147_1115	235.9°	x	x	x	x
	ESP_030002_1115	228.8°	x	x	x	x
	ESP_029936_1115	225.6°	x	x	x	x
	ESP_029725_1115	215.4°		x	x	x
	ESP_029580_1115	208.5°		x	x	x
	ESP_029369_1115	198.7°		x	x	x
	ESP_029079_1115	185.5°		x	x	x
	ESP_029013_1115	182.6°	x	x	x	x
	ESP_028802_1115	173.3°	x	x	x	x
	ESP_028657_1115	167.2°	x	x	x	x
	ESP_028446_1115	158.4°	x	x	x	x
MY30	ESP_023646_1115	243.8°	x	x	x	x
	ESP_022156_1115	276.6°	x	x	x	x
	ESP_021668_1115	252.6°	x	x	x	x
	ESP_021589_1115	248.7°	x	x	x	x
	ESP_020956_1115	217.7°	x	x	x	x
MY29	ESP_013585_1115	288.4°	x	x	x	x
	ESP_013097_1115	264.7°	x	x	x	x
	ESP_012741_1115	247.1°	x	x	x	x
	ESP_012332_1115	227°	x	x	x	x
	ESP_012319_1115	226.4°		x	x	x
	ESP_011963_1115	209.3°	x	x	x	x
	ESP_011752_1115	199.4°	x	x	x	x
	ESP_011607_1115	192.7°	x	x	x	x
	ESP_011396_1115	183.2°	x	x	x	x
	PSP_010829_1115	159°	x	x	x	x
MY28	PSP_003511_1115	226.7°	x	x	x	x
	PSP_003287_1115	215.9°	x	x	x	x

Site 2	**HiRISE image**	**Ls**	**Site 2**
MY35	ESP_065342_1090	232.5°	x
MY34	ESP_058406_1090	322.3°	x
	ESP_057773_1090	293.4°	x
	ESP_057219_1090	266.7°	x
	ESP_057008_1090	256.2°	x

MY33	ESP_048608_1090	276.7°	x
MY32	ESP_039747_1090	274.6°	x
	ESP_039536_1090	264.2°	x
	ESP_039325_1090	253.8°	x
	ESP_037584_1090	171.9°	x
MY31	ESP_030859_1090	271.1°	x
	ESP_030424_1090	249.6°	x
	ESP_029224_1090	192°	x
	ESP_028868_1090	176.2°	x
	ESP_028512_1090	161.1°	x
MY30	ESP_023290_1090	328.9°	x
MY29	ESP_013875_1095	302.1°	x
	ESP_013163_1090	268.0°	x
	ESP_012530_1090	236.7°	x
	ESP_011673_1090	195.7°	x
MY28	PSP_005621_1090	327.2°	x
	PSP_003498_1090	226.1°	x
	PSP_003353_1090	219.1°	x
	PSP_002786_1090	192.5°	x
Site 3	**HiRISE image**	**Ls**	**Site 3**
MY35	ESP_065725_1105	251.3°	x
	ESP_065303_1105	230.5°	x
	ESP_064881_1105	210.2°	x
	ESP_064037_1105	172°	x
MY34	ESP_057734_1105	291.6°	x
	ESP_056072_1105	210.5°	x
	ESP_055584_1105	188°	x
MY33	ESP_048780_1105	285°	x
	ESP_048424_1105	267.7°	x
	ESP_047844_1105	239.1°	x
	ESP_047567_1105	225.2°	x
	ESP_047422_1105	218.5°	x
	ESP_047211_1105	208.4°	x
	ESP_046710_1105	185.4°	x
	ESP_046644_1105	182.4°	x
	ESP_046433_1105	173.2°	x
	ESP_046288_1105	167.1°	x
MY32	ESP_040486_1105	309.5°	x
	ESP_039286_1105	251.9°	x
	ESP_038732_1105	224.6°	x
	ESP_038389_1105	208.2°	x
	ESP_038178_1105	198.3°	x
	ESP_037624_1105	173.6°	x
	ESP_037479_1105	167.4°	x
MY31	ESP_032455_1105	343.5°	x
	ESP_030886_1105	272.4°	x

	ESP_030609_1105	258.8°	x
	ESP_030174_1105	237.3°	x
	ESP_030108_1105	234°	x
	ESP_029897_1105	223.7°	x
	ESP_029686_1105	213.6°	x
	ESP_029475_1105	203.6°	x
	ESP_029396_1105	199.9°	x
	ESP_028974_1105	180.8°	x
	ESP_028618_1105	165.5°	x
MY30	ESP_021840_1105	261.1°	x
	ESP_020205_1105	182.9°	x

Supplementary Table S2: Frost evolution for areas C and D of site n°1: 68.5°S and 1.3°E (Fig. 1B).

		Translucent frost	Dark spots/dark flows	Beginning of defrosting	Bright frost (first appears)	bright frost throughout	No frost
Area C	**MY29**	159° to 227°	159° to 227° (few at 183.2°) and patchy at 247.1°	226.4°	226.4°	from 247.1°	from 264.7° to 288.4°
	MY31	158.4° to 215.4°	158.4° to 215.4° and patchy from 225.6° to 235.9°	225.6°	225.6° and 228.8°	from 235.9°	263.3°
	MY32	160.2° to 210°	160.2° to 210° (numerous Ls 166.3° and 178.1°) and 243.4° (some)	No data	No data	243.4°	268.1°
	MY33	159.9° to 220.4°	159.9° to 220.4° (numerous Ls 174.8° and 177.8°)	220.4°	226.8°	from 234.5° and 252.1°	300.6°
	MY34	183.3° to 202.5°	183.3° to 202.5° (few at Ls 192.7° and 202.3°) and 215.6° and 242.6°	No data	215.6°	from 232.2° to 242.6°	292.3°
Area D	**MY29**	159° to 209.3°	159° and 183.2°	183.2°	from 226.4° to 227°	No data	from 247.1° to 288.4°
	MY31	158° to 208.5°	158.4° to 173.3°	167.2°		from 215.4° to 235.9°	from 253.5° to 263.3°
	MY32	160.2° to 210°	numerous (Ls 160.2°) and few from Ls 160.2° to 178.1°	178.1°	210°	No data	from 243.4° to 268.1°
	MY33	159.9° to 200.4°	numerous (Ls 159.9°). few at Ls 174.9° and 177.8°	174.9°	210.3°	from 220.4° to 234.5°	300.6°
	MY34	183.3° to 202.5°	No data	No data	from 215.6° to 242.6°	from Ls 215.6° to 242.6°	290.3°

Supplementary Table S3: location and type of defrosting for areas C and D for the site n°1: 68.5°S and 1.3°E (Fig. 1B).

		Frost visible on all surfaces (gullies and surroundings)	Alcoves begin to defrost equator-facing	Alcove defrosting (in progress)	Channel and apron defrosting (in progress)	Complete defrosting of gully surroundings	No frost
Area C	**MY29**	from 159° to 209.3°	226.4°	247.1°	247.1°	247.1°	from 264.7° to 288.4°
	MY31	from 158.4° to 215.4°	225.6°	235.9°	No data	235.9°	from 253.5° to 263.3°
	MY32	from 160.2° to 210°		243.4°	243.4°	No data	268.1°
	MY33	from 159.9° to 210.3°	220.4°	252.1°	252.1°	220.4°	252.1°
	MY34	from 183.3° to 215.6°	232.2°	242.6°	242.6°	232.2°	290.3°
Area D	**MY29**	159°	No data	from 159° to 227° (acceleration from Ls 209.3°) (159° to 199.4°, slower defrost)	No data	227°	from 247.1° to 288.4°
	MY31	158.4°	No data	from 167.2° to 225.6° (from 167.2° to 185.5° slight defrosting and, more complete at 225.6°	from 228.8° to 235.9°	225.6°	253.5°
	MY32	From 160.2° to 166.3°	No data	from 178.1° to 203.2° (acceleration)	No data	No data	243.4°
	MY33	159.9°	No data	from 174.9° to 200.4° (more widespread at 200.4°)	226.8 to 234.5°	210.3°	300.6°
	MY34	No data	No data	from 183.3° and more widespread at 202.5°	232.2°	215.6°	242.6°

Supplementary Table S4: Defrosting sequence observed for areas A. B. C and D (site n°1: 68.5°S and 1.3°E) in MY 31 (Fig. 1B).

		Orientation	Translucent frost	Dark spots/dark flows	Beginning of defrosting	Bright frost (begins to form)	bright frost throughout	No frost
MY31	**Area A**	80°-85°N	from Ls 158.4° to 182.6°	from Ls 158.4° to 182.6° and patchy from Ls 225.6° to 235.9°	No data	No data	from Ls 225.6° to 235.9°	from Ls 253.5° to 263.3°
	Area B	95°-105°N	from Ls 158.4° to 228.8°	from Ls 158.4° to 228.8° numerous dark spots Ls 167.2° and 173.3° and numerous dark flows at Ls 215.4° and 225.6°	Ls 198.4°	from Ls 225.6° to 263.3°	No data	from Ls 288.3° to 321°
	Area C	130°-140°N	from 158.4° to 228.8°	overall few from 158.4° to 228.8° (except numerous dark spots at Ls 167.2° and 173.3° and dark flows at Ls 215.4° and 225.6°)	Ls 225.6°	from 225.6° to 263.3°	No data	From Ls 288.3° to 321°

	Area D	0°-10°N	from Ls 158.4° to Ls 208.5°	Few from Ls 158.4° to 173.3°	Ls 182.6°	No data	from Ls 215.4° to 235.9°	from Ls 253.5° to 263.3°

Supplementary Table S5: Distribution of frost inside gullies for MY31 for the areas A, B, C and D (site n°1: 68.5°S and 1.3°E) (Fig. 1B). (Yes/No = frost present (or not) on the surface named in the column).

	Frost on all surfaces	Frost on gully-alcove	Frost on gully-channel	Frost on gully-apron	Frost around gullies
MY31 area A					
Ls 263.3°	No	No	No	No	No
253.5°	No	No	No	No	No
235.9°	No	nearly completely defrosted (except the lower part of the alcove)	defrosting is advanced: all equator-facing slopes and only some patches of frost are present on pole-facing slopes	Yes	advanced defrost
228.8°	No	alcove slopes facing the equator are defrosted	numerous slopes facing the equator are defrosted and some small patches begin to defrost facing the pole	Yes	Yes
225.6°	No	alcove slopes facing the equator are defrosted	numerous equator- facing slopes are defrosted	Yes	Start of defrosting around gullies
215.4-185.5°	No image	No image	No image	No image	No image
182.6°	Yes	Yes	Yes	Yes	Yes
173.3°	Yes	Yes	Yes	Yes	Yes
167.2°	Yes	Yes	Yes	Yes	Yes
158.4°	Yes	Yes	Yes	Yes	Yes
MY31 area B					
Ls 263.3°	No	No	No	No	No
253.5°	No	No	No	No	No
235.9°	No	equator-facing slopes are defrosted and defrosting beginning on pole-facing slopes	defrosting starting on equator-facing slopes	Yes	defrosted
228.8°	No	equator-facing slopes continuing to defrost	defrosting starting on equator-facing slopes	Yes	defrost in progress
225.6°	No	equator-facing slopes continuing to defrost	defrosting starting on equator-facing slopes	Yes	defrosting starting
215.4°	No	equator-facing slopes continuing to defrost	Yes	Yes	Yes
208.5°	No	equator-facing slopes continuing to defrost	Yes	Yes	Yes
198.7°	No	patchy defrost of equator-facing slopes	Yes	Yes	Yes
185.5°	Yes	Yes	Yes	Yes	Yes
182.6°	Yes	Yes	Yes	Yes	Yes
173.3°	Yes	Yes	Yes	Yes	Yes
167.2°	Yes	Yes	Yes	Yes	Yes

158.4°	Yes	Yes	Yes	Yes	Yes
MY31 area C					
Ls 263.3°	No	No	No	No	No
253.5°	No	No	No	No	No
235.9°	No	defrosting underway for equator-facing slopes and patchy defrosting for pole-facing slopes	patchy defrosting on equator-facing slopes and some small patches of defrosting on pole-facing slopes	Yes	defrosting advanced
228.8°	No	defrosting only on equator-facing slopes	some very small patches of defrosting inside channel for equator-facing slopes	Yes	Yes
225.6°	No	defrosting only on equator-facing slopes	some very small patches of defrosting inside channel for equator-facing slopes	Yes	Yes
215.4°	Yes	Yes	Yes	Yes	Yes
208.5°	Yes	Yes	Yes	Yes	Yes
198.7°	Yes	Yes	Yes	Yes	Yes
185.5°	Yes	Yes	Yes	Yes	Yes
182.6°	Yes	Yes	Yes	Yes	Yes
173.3°	Yes	Yes	Yes	Yes	Yes
167.2°	Yes	Yes	Yes	Yes	Yes
158.4°	Yes	Yes	Yes	Yes	Yes
MY31 area D					
Ls 263.3°	No	No	No	No	No
253.5°	No	No	No	No	No
235.9°	No	No	really advanced defrosting	almost completely defrosted	almost completely defrosted
228.8°	No	No	Defrosting started	Defrosting starting	defrosting in progress
225.6°	No	No	Yes	Yes	defrosting in progress
215.4°	No	defrosting on the upper part of the alcove (on equator-facing slopes)	Yes	Yes	advanced defrosting
208.5°	No	frost on the upper part of the alcove follow to defrost and also surface between gullies (when they are slopes face to equator)	Yes	Yes	Yes
198.7°	No	frost on the upper part of the alcove only and defrsoted surface between gullies (facing equatorwards)	Yes	Yes	Yes
185.5°	No	defrosting in progress in upper part of the alcove on equator-facing slopes	Yes	Yes	Yes
182.6°	No	defrosted on all upper part of the alcove (face to equator)	Yes	Yes	Yes
173.3°	No	defrosting begins slopes oriented toward the equator: all upper part of the alcove defrosted	Yes	Yes	Yes
167.2°	Yes	Yes	Yes	Yes	Yes
158.4°	Yes	Yes	Yes	Yes	Yes

945

Supplementary Table S6: Evolution of dark spots and dark flows for the areas A. B. C and D (site n°1: 68.5°S and 1.3°E) (Fig. 1B). (Yes = dark spots/flows present, No = dark spots/flows not present and no image = no available image).

	Dark spots/flows present on gully-alcove	Dark spots/flows present on gully-channel	Dark spots/flows present on gully-apron	Dark spots/flows present on the edge of gully-apron	Dark spots/flows present around gullies
MY31 area C					
Ls 263.3°	No	No	No	No	No
253.5°	No	No	No	No	No
235.9°	No	No	Yes (few on recently active part of apron)	No	No
228.8°	No	No	No	No	No
225.6°	No	Yes (very few)	No	No	No
215.4°	No	Yes (few)	Yes (few)	No	No
208.5°	No	Yes (few)	Yes (few)	No	No
198.7°	No	Yes (few)	Yes (few)	No	No
185.5°	No	Yes (few)	Faded	Faded	Faded
182.6°	No	Yes (few)	Faded	Faded	Faded
173.3°	No	Yes (with growth and some beginning to fade)	Yes (on active apron) with growth and some beginning to fade	Yes (more)	Yes (more)
167.2°	No	Yes (with growth and some beginning to fade)	Yes (on active apron) with growth and some beginning to fade	Yes	Yes
158.4°	No	Yes	Yes (on active apron)	No	Yes (Beyond gully apron, patchy)
MY31 area B					
Ls 263.3°	No	No	No	No	No
253.5°	No	No	No	No	No
235.9°	No	No	Yes (reappear on the active apron)	No	No
228.8°	No	Yes (continuing to fade)	Yes (continuing to fade on active apron)	No	No
225.6°	No	Yes (continuing to fade)	Yes (continuing to fade on active apron)	No	No
215.4°	No	Yes (faded)	Yes (faded on active apron)	No	No
208.5°	No	Yes (few)	Yes (very few on active apron.)	No	No
198.7°	No	Yes (few)	Yes (very few on active apron.)	No	No
185.5°	No	Yes (few)	Yes (very few on active apron), faded for the rest of the apron	No	No
182.6°	No	Yes (few)	Faded	Faded	Faded
173.3°	No	Yes (more present and continuing to fade)	Yes (on active apron) growth and continuing to fade; few on apron in general progress and beginning to fade	Yes (growth and beginning to fade)	Yes (growth and beginning to fade)
167.2°	No	Yes (more present and beginning to fade)	Yes (on active apron) growth and beginning to fade; few on apron in general	Yes	Yes

158.4°	No	Yes	Yes (on active apron)	No	Yes (patchy)
MY31 area A					
Ls 263.3°	No	No	No	No	No
253.5°	No	No	No	No	No
235.9°	No	No	No	No	No
228.8°	No	No	No	No	No
225.6°	No	No	No	No	No
215.4°	no image	no image	no image	no image	no image
208.5°	no image	no image	no image	no image	no image
198.7°	no image	no image	no image	no image	no image
185.5°	no image	no image	no image	no image	no image
182.6°	No	Yes	Yes (only few faded in places)	No	No
173.3°					
167.2°	No	Yes (more present and beginning to fade)	Yes (mainly on the active apron: growth and beginning to fade); on the apron in general	Yes (growth and beginning to fade)	Yes (growth and beginning to fade)
158.4°	No	Yes	Yes (mainly on the active apron)	Yes	Yes
MY31 area D					
Ls 263.3°	No	No	No	No	No
253.5°	No	No	No	No	No
235.9°	No	No	No	No	No
228.8°	No	No	No	No	No
225.6°	No	No	No	No	No
215.4°	No	No	No	No	No
208.5°	No	No	No	No	No
198.7°	No	No	No	No	No
185.5°	No	No	No	No	No
182.6°	No	No	No	No	No